โครงสร้างนาโนของอินเดียมแกลเลียมอาร์เซไนด์ที่ปลูกผลึกด้วยวิธีดรอปเล็ทอิพิแทกซีจากลำโมเลกุล

นางสาวนราพร ปั้นเก่า

วิทยานิพนธ์นี้เป็นส่วนหนึ่งของการศึกษาตามหลักสูตรปริญญาวิศวกรรมศาสตรมหาบัณฑิต
สาขาวิชาวิศวกรรมไฟฟ้า ภาควิชาวิศวกรรมไฟฟ้า
คณะวิศวกรรมศาสตร์ จุฬาลงกรณ์มหาวิทยาลัย
ปีการศึกษา 2549

InGaAs NANOSTRUCTURES GROWN BY DROPLET MOLECULAR BEAM EPITAXY

Miss Naraporn Pankaow

A Thesis Submitted in Partial Fulfillment of the Requirements
for the Degree of Master of Engineering Program in Electrical Engineering
Department of Electrical Engineering
Faculty of Engineering
Chulalongkorn University
Academic year 2006

หัวข้อวิทยานิพนธ์	โครงสร้างนาโนของอินเดียมแกลเลียมอาร์เซไนด์ที่ปลูกผลึกด้วยวิธีดรอปเล็ทอิพิแทกซีจากลำโมเลกุล
โดย	นางสาวนราพร ปิ้นเก่า
สาขาวิชา	วิศวกรรมไฟฟ้า
อาจารย์ที่ปรึกษา	ศาสตราจารย์ ดร. สมศักดิ์ ปัญญาแก้ว
อาจารย์ที่ปรึกษาร่วม	รองศาสตราจารย์ ดร. สมชัย รัตนธรรมพันธ์

คณะวิศวกรรมศาสตร์ จุฬาลงกรณ์มหาวิทยาลัย อนุมัติให้นับวิทยานิพนธ์ฉบับนี้เป็นส่วนหนึ่งของการศึกษาตามหลักสูตรปริญญามหาบัณฑิต

..... คณบดีคณะวิศวกรรมศาสตร์
(ศาสตราจารย์ ดร. ดิเรก ลาวัณย์ศิริ)

คณะกรรมการสอบวิทยานิพนธ์

..... ประธานกรรมการ
(รองศาสตราจารย์ ดร. มนตรี สวัสดิ์ศฤงฆาร)

..... อาจารย์ที่ปรึกษา
(ศาสตราจารย์ ดร. สมศักดิ์ ปัญญาแก้ว)

..... อาจารย์ที่ปรึกษาร่วม
(รองศาสตราจารย์ ดร. สมชัย รัตนธรรมพันธ์)

..... กรรมการ
(รองศาสตราจารย์ ดร. บรรยง โตประเสริฐพงศ์)

..... กรรมการ
(อาจารย์ ดร. สกุลธรรม เสนาะพิมพ์)

นราพร ปิ้นเก่า : โครงสร้างนาโนของอินเดียมแกลเลียมอาร์เซไนด์ที่ปลูกผลึกด้วยวิธีดรอปเล็ทอิพิแทกซีจากลำโมเลกุล. (InGaAs NANOSTRUCTURES GROWN BY DROPLET MOLECULAR BEAM EPITAXY) อ. ที่ปรึกษา : ศ.ดร. สมศักดิ์ ปัญญาแก้ว, อ. ที่ปรึกษาร่วม : รศ.ดร. สมชัย รัตนธรรมพันธ์, 72 หน้า.

วิทยานิพนธ์ฉบับนี้ นำเสนอการปลูกโครงสร้างนาโนรูปวงแหวนของอินเดียมแกลเลียมอาร์เซไนด์ด้วยวิธีดรอปเล็ทอิพิแทกซีจากลำโมเลกุล โดยมีการแปรเงื่อนไขในการขึ้นรูปหยดของอินเดียมแกลเลียม เพื่อศึกษาผลของอุณหภูมิแผ่นฐานขณะปลูกอินเดียมแกลเลียมและปริมาณอินเดียมแกลเลียมที่ปลูกลงไปที่มีต่อโครงสร้างนาโนรูปวงแหวนของอินเดียมแกลเลียมอาร์เซไนด์ พบว่าเมื่ออุณหภูมิแผ่นฐานขณะปลูกอินเดียมแกลเลียมสูงขึ้นจะทำให้ขนาดของโครงสร้างอินเดียมแกลเลียมอาร์เซไนด์รูปวงแหวนมีขนาดใหญ่ขึ้น แต่ค่าความหนาแน่นของจำนวนโครงสร้างนาโนลดลง เนื่องจากระยะการแพร่กระจายของอะตอมโลหะอินเดียมและแกลเลียมมีค่าเพิ่มขึ้นส่งผลทำให้หยดของอินเดียมแกลเลียมแผ่ขยายไปในทิศทางสองมิติและรวมตัวกับหยดที่อยู่ใกล้เคียง ในทางเดียวกันการเพิ่มปริมาณอินเดียมแกลเลียมที่ปลูกลงไปทำให้ขนาดของโครงสร้างอินเดียมแกลเลียมอาร์เซไนด์รูปวงแหวนมีขนาดใหญ่ขึ้น ค่าความหนาแน่นของโครงสร้างนาโนรูปวงแหวนก็มีค่าเพิ่มขึ้นเช่นกันเมื่อเพิ่มปริมาณอินเดียมแกลเลียมระหว่าง 2-3 โมโนเลเยอร์ (monolayer, ML) แต่เมื่อเพิ่มปริมาณอินเดียมแกลเลียมเป็น 4 โมโนเลเยอร์ ค่าความหนาแน่นของจำนวนโครงสร้างวงแหวนกลับลดลง และเพิ่มขึ้นอีกครั้งเมื่อเพิ่มปริมาณอินเดียมแกลเลียมเป็น 5 โมโนเลเยอร์ การที่ค่าความหนาแน่นลดลงนี้คาดว่าเกิดจากการก่อตัวเป็นชั้นเรียบของอินเดียมแกลเลียมแทนที่จะเกิดเป็นหยดอินเดียมแกลเลียมเดี่ยวๆ เมื่อเพิ่มปริมาณของอินเดียมแกลเลียมที่ปลูกลงไป ดังนั้นอะตอมอินเดียมแกลเลียมที่ปลูกตามลงไป จะก่อตัวเป็นหยดขึ้นเหนือชั้นเรียบนั้น ทำให้จำนวนของหยดที่ปรากฏลดลงไปใหม่

สำหรับการวัดคุณสมบัติทางแสงของโครงสร้างนาโน โครงสร้างนาโนรูปวงแหวนของอินเดียมแกลเลียมอาร์เซไนด์ถูกประดิษฐ์ขึ้นอีกครั้งภายใต้เงื่อนไขที่เลือกและปลูกกลบด้วยชั้นของแกลเลียมอาร์เซไนด์หนา 100 นาโนเมตร อันประกอบด้วยชั้นแกลเลียมอาร์เซไนด์ที่ปลูกด้วยโดยวิธีไมเกรชัน-เอนฮานซ์อิพิแทกซี (migration-enhanced epitaxy) และชั้นแกลเลียมอาร์เซไนด์ที่ปลูกด้วยวิธีทั่วไป คุณสมบัติทางแสงของโครงสร้างรูปวงแหวนของอินเดียมแกลเลียมอาร์เซไนด์สังเกตได้จากการเปล่งแสงของตัวอย่าง เมื่อชิ้นงานดังกล่าวได้รับการกระตุ้นจากแสง (PL spectra) ที่อุณหภูมิ 77 เคลวิน ซึ่งแสดงถึงผลึกที่ได้นั้นมีคุณสมบัติที่ดี แต่อย่างไรก็ตามค่าความเข้มของแสงที่ได้ยังมีค่าไม่มากนัก เนื่องจากมีค่าความหนาแน่นของจำนวนโครงสร้างวงแหวนของอินเดียมแกลเลียมอาร์เซไนด์ที่ต่ำ (10^8 cm^{-2})

ภาควิชา .....วิศวกรรมไฟฟ้า..... ลายมือชื่อนิสิต .....

สาขาวิชา .....วิศวกรรมไฟฟ้า..... ลายมือชื่ออาจารย์ที่ปรึกษา .....

ปีการศึกษา .....2549..... ลายมือชื่ออาจารย์ที่ปรึกษาร่วม .....

4870675021 : MAJOR ELECTRICAL ENGINEERING
KEY WORD: InGaAs / GaAs / NANOSTRUCTURES / DROPLET / MOLECULAR BEAM EPITAXY

NARAPORN PANKAOW : InGaAs NANOSTRUCTURES GROWN BY DROPLET MOLECULAR BEAM EPITAXY, THESIS ADVISOR : PROF. SOMSAK PANYAKEOW, D.Eng., THESIS CO-ADVISOR : ASSOC. PROF. SOMCHAI RUTANATHUMMAPHAN, D.Eng., 72 pp.

InGaAs ring-shaped nanostructures are fabricated by droplet epitaxy technique using solid source molecular beam epitaxy (MBE). InGa droplet forming conditions have been varied in order to investigate the effect of substrate temperature during InGa deposition and deposited amount of indium (In) and Gallium (Ga) on InGaAs ring-structures. It was found that increasing substrate temperature during InGa deposition resulted in InGaAs rings larger size but lower density since greater diffusion length of metallic In and Ga atoms responsed to 2-dimensional expansion of InGa droplets and coalescence of neighbouring droplets. Also, the increasing InGa amount deposited would result in InGaAs rings larger size. The ring density is also increased when increasing InGa amount between 2-3 ML. However, when increasing InGa amount to 4 ML, the density becomes to decrease. The density is increased again while increasing InGa amount to 5 ML. It was supposed that decrease of ring density was caused from formation of InGa full-layer instead of individual droplets when greater amount of InGa was deposited. Subsequently, newly supplied InGa adatoms would form the droplets above the layer resulting in renewal of the number of the droplet formed.

For photoluminescence (PL) measurement, the nanostructures were repeatedly grown under selected droplet forming condition with additional 100-nm GaAs capping layers including GaAs layers grown by migration-enhanced epitaxy and conventional GaAs layers. The analytical optical properties of InGaAs rings are confirmed by the PL spectra of capped InGaAs ring-structures at 77K. The PL result indicates the high quality crystal. However, PL intensity was found to be low resulting from low density of the ring structures (10^8 cm^{-2}).

Department ..Electrical Engineering...	**Student's signature** .....
Field of study Electrical Engineering...	**Advisor's signature** .....
Academic year .....2006.....	**Co-advisor's signature** .....

Acknowledgements

The author would like to give special thanks to his family for endless and encouraging support throughout this work.

The author gratefully acknowledges all those who provided invaluable help and encouragement during the research at the Semiconductor Device Research Laboratory (SDRL), Department of Electrical Engineering, Faculty of Engineering, Chulalongkorn University, Bangkok, Thailand. In particular, the author would like to acknowledge to Professor Dr. Somsak Panyakeow, and Associate Professor Dr. Somchai Ratanathammaphan, who are the advisor and co-advisors. Moreover, this thesis could not have been completed without special helps of SDRL researcher : Mr. Supachok Thainoi, and her colleagues.

Finally, the author is grateful to Thailand Research Fund (TRF), National Technology and Science Development Agency (NTSDA) through National Nanotechnology Center (Nanotec), Ministry of Education through Commission of Higher Education (CHE), and Chulalongkorn University for financial support from.

CONTENTS

Page

LIST OF FIGURES

Figure Page

Figure Page

Figure Page

Figure Page

Figure Page

LIST OF SYMBOLS

∇^2	Laplacian operator
A	surface area
AFM	atomic force microscopy
Al	aluminium
AlAs	aluminium arsenide
AlP	aluminium phosphide
As	arsenic
BEP	beam equivalent pressure
CB	conduction band
δ	delta function
Δ	total spectrum broadening from all excited quantum dot
$\Delta\gamma$	change of surface free energy
$D_{\text{bulk}}(E)$	bulk density of state
$D_{\text{QW}}(E)$	quantum well density of state
$D_{\text{QWR}}(E)$	quantum wire density of state
$D_{\text{QD}}(E)$	quantum dot density of state
D.O.S.	density of state
ε	misfit
ε_0	lattice mismatch
E	carrier energy
	or total energy per unit cell
E_g	band gap energy
$E_{n,x}$	quantized energy in x-direction
$E_{n,y}$	quantized energy in y-direction
$E_{n,z}$	quantized energy in z-direction
E(el)	elastic strain energy
F	free energy
$F(\mathbf{r})$	envelope wave function
FM	Frank van der Merwe
FWHM	full width at half maximum
γ_e	surface free energy of the epilayer/vacuum interface

γ_i	surface free energy of epilayer/substrate interface
γ_S	surface free energy of the substrate/vacuum interface
g^{sat}	maximum optical gain
Ga	gallium
GaAs	gallium arsenide
GaP	gallium phosphide
h	Planck's constant
$\hbar$	reduced Planck's constant
H_2O	water
$I(\Phi)$	persistent current of a quantum ring
In	indium
InAs	indium arsenide
InGaAs	indium gallium arsenide
InGaP	indium gallium phosphide
InP	indium phosphide
k	amplitude of wave vector
k_B	Boltzmann's constant
$k_{//}$	amplitude of in-plane (y-z) wave vector
$k_{\perp}$	amplitude of wave vector in x-direction
$\mathbf{k} = (k_x, k_y, k_z)$	carrier wave vector
λ	elastic modulus
$\lambda_{\text{de Broglie}}$	de Broglie wavelength
L	macroscopic length scale
L_{QW}	sum of the well and barrier regime thickness
L_x	nanometer length scale in x direction
L_y	nanometer length scale in y direction
L_z	nanometer length scale in z direction
m^*	effective mass
m_{eff}	carrier effective mass
MBE	molecular beam epitaxial or molecular beam epitaxy

ML	monolayer
Mo	molybdenum
n	quantum number in z-direction (integer)
N_2	nitrogen
N_D	volume density of quantum dot
N_e	number of state per unit surface
N_{wi}	area density of quantum wire
p	carrier momentum
PBN	pyrolytic boron nitride
PL	photoluminescence
QW	quantum well
QWR	quantum wire
QD	quantum dot
RHEED	reflection high-electron energy diffraction
Si	silicon
SiGe	silicon germanium
SK	Stranski Krastanow
Θ	Heaviside's unit step function
t	film thickness
T	temperature
UHV	ultra high vacuum
$V(\mathbf{r})$	confinement potential
VM	Volmer Weber
WL	wetting layer
X_{Out}	outer diameter of ring-shaped nanostructures
Z	height of ring-shaped nanostructures
Φ	magnetic flux piercing a ring
θ	angle

CHAPTER I

INTRODUCTION

1.1 Motivation

The fabrication of quantum-confined nanostructures by self-assembling growth methods has been intensively investigated in the last decade for basic physic and device application [1-3] especially in opto-electronic such as laser, detector and solar cell. Their atom-like properties of electron confinement and energy level quantization response to the emission of certain-energy photon when the nanostructures are stimulated. Among them, semiconductor quantum rings have attracted a great deal of attention because fascinating properties have been predicted and demonstrated [4, 5]. Ring-shaped nanostructures, so called quantum rings, are a special class of quantum-confinement structures that have attracted a lot of attention due to the Aharonov-Bohm effect [6], which is a specific to the topology of a ring. Particularly interests are the magnetic properties of such quantum systems which are related to the possibility of inducing persistent currents.

In recent years, the fabrication and investigation of self-assembled InAs quantum-rings have been rapidly progressing and led to large number of theoretical and experimental studies. Recently, various fabrication technique for quantum-ring have been developed. Stranski-Krastanow (SK) growth mode has become extremely attractive in the case of a lattice-mismatched system, that is, the nanostructures are resulted from releasing strain caused by lattice-mismatch between the substrate and the overlayer [2, 3, 7, 8] such as InAs/GaAs and InGaAs/GaAs systems by capping self-assembled quantum-dot with a thin layer [9]. However, the size of the quantum dots fabricated by SK growth mode are widely distributed, resulting in luminescence peak boarding [10, 11]. Moreover, it has been point out that the non-uniform strain distribution in this lattice-mismatched system would effect on the band structure. It is undesirable for laser applications. From the viewpoint, well-defined strain-free ring structures are desirable for studies of the physics of semiconductor quantum rings. For the growth of high-quality self-assembled nanostructures in lattice-matched systems,

droplet epitaxy is a promising method [1, 12]. While droplet epitaxy has been used only for quantum dot (QD) fabrication, this method has potential for the growth of more complex nanostructures [13, 14].

Droplet epitaxy is an alternative approach of self-organized nanostructure fabrication which can be applied to both lattice-matched and mismatched systems. Unlike the SK growth mode, the nanostructures fabricated by droplet epitaxy are originated from group III-element droplets formed on III-V compound substrate. Since the droplets of group III-element are uniform, the uniform-size nanostructures can be formed [1, 11, 15-17]. Furthermore, the lattice-matched system in droplet formation would reduce the strain-energy in the nanostructures and its effects on the energy-band structure.

However, the fabrication of InAs nanostructures by droplet epitaxy on GaAs substrates still has some problems such as relative low density and large size [18] due to too long two-dimensional migration length of In atoms and high segregation effect of the newly supplied adatoms, and worse optical quality. A solution to overcome the problems is growth at low temperature and using optimum crystallization conditions [19]. To restrict the migration (diffusion) length of In atom on GaAs substrate, Ga of which lattice is mostly matched to GaAs is also supplied during the deposition of In [20]. The droplets of InGa are formed instead. This would also results in the formation of InGaAs nanostructures after the crystallization instead of InAs nanostructures.

In this work, InGaAs ring-like nanostructures were fabricated by droplet molecular beam epitaxy. The droplet forming conditions have been varied by varying substrate temperature during depositing InGa and InGa amount deposited. The surface morphology are characterized by atomic force microscopy (AFM) for analyzing the size and density of the ring structures fabricated under each droplet forming condition. The dependence of InGaAs ring-shaped nanostructures on substrate temperature and amount of InGa deposited was investigated. For photoluminescence (PL) measurement, the InGaAs ring-structures were repeatedly grown under selected droplet forming condition with additional 100-nm GaAs capping layers. The capping layers included 50 ML of GaAs layers grown by migration-enhanced epitaxy [21, 22] at 350°C in order to grow the high quality capping layers at low growth temperatures, and 310 ML of conventional GaAs layers grown at 400°C respectively. The analytical optical properties of the InGaAs ring-shaped nanostructures are confirmed

by the PL spectra of respective capped InGaAs ring-structures at 77K showing the PL peak and respective PL full width at half maximum (FWHM).

1.2 Objective

This thesis objective is to study the fabrication of InGaAs nanostructures on GaAs by droplet molecular-beam epitaxy under varied droplet forming conditions. To vary the conditions, we have varied the droplet forming parameter, including amount of InGa deposited (equivalent to droplet layer thickness) and substrate temperature while depositing droplets. Next, the surface morphology of grown InGaAs nanostructures has been examined in order to analyze the effect of each droplet forming parameter on the size and density of the nanostructures. For PL measurement, the nanostructures have been re-fabricated under selected droplet forming condition with additional GaAs capping layers. The analytical optical properties of the nanostructures have been investigated from PL spectra of GaAs-capped InGaAs-nanostructure sample at 77K.

1.3 Overview

This thesis presents a detailed study of the fabrication of InGaAs ring-shaped nanostructures by droplet epitaxy using molecular beam epitaxy (MBE). The purpose is to analyze the effect of droplet forming parameters on the size and density of the nanostructures. Moreover, the photoluminescence of InGaAs ring-shaped nanostructures has been presented.

The thesis is organized as follows: The basic concepts of low-dimensional nanostructures are reviewed in chapter 2. This also includes fabrication techniques for nanostructure formation. Chapter 3 gives the experimental details. In chapter 4, experimental results from the fabrication of InGaAs ring-shaped nanostructures are presented. The effects of InGa amount deposited, and substrate temperature on size and density of InGaAs nanostructures are studied in this chapter. The studies are based on atomic force microscopy (AFM) and photoluminescence (PL) results. Finally, chapter 5 concludes this work.

CHAPTER II

LOW-DIMENSIONAL NANOSTRUCTURES

The basic concepts of quantum dot (QD) structure, which is a low-dimensional semiconductor nanostructure, are reviewed in this chapter. A comparison of important intrinsic properties of nanostructures is presented. The properties of ring-shaped nanostructures, a type of quantum-confinement structures, are also reviewed to be useful for the interpretation of nanostructure characteristics.

In another part of this chapter, self-assembled growth of the nanostructures is presented based on epitaxial growth. SK growth mode is briefly introduced to provide basic of QD formation from strain-releasing in lattice mismatch system. The next section, a review of droplet epitaxy which is the lattice-matched method used to fabricate the ring-shaped nanostructures in this research work is presented. Finally, the information of the material system which is used to create the nanostructures is provided.

2.1 Basic concepts of low-dimensional nanostructures

The band theory of crystals has been rigidly developed from the quantum theory for atoms since the last century [23, 24]. From the quantum theory, we know that when we place atoms, which have discrete energy levels, together then they become solid. The energy levels of solid crystal become energy bands. From the engineering point of view the most relevant bands are the conduction band and the valence band which are separated in energy by the band gap. The conduction band is free of electrons at 0 K, while the valence band is full with electron at 0 K. At $T > 0$ K, these two bands are partially filled with electrons and holes, which act as charge carriers in devices operations. Controlling the carrier motion in these two bands is the subject of band gap engineering. We, therefore, consider only these two bands.

In this section, the important properties of nanostructures are reviewed. Since nanostructures with low-dimensional shapes provide the potential well resulted from difference of energy band gap (E_g) of 2 materials, the carriers (electrons and holes)

can be confined and results in a quantization of carrier energy. Therefore, the certain-energy photon would be emitted when nanostructures are stimulated.

2.1.1 Carrier confinement and energy level quantization

In low-dimensional nanostructures large carriers are confined in one or more directions and the length scale of confining direction is in the order of the de Broglie wavelength (carrier wavelength). The de Broglie wavelength, $\lambda_{\text{de Broglie}}$, depends on the carrier effective mass, m^*, and temperature, T [25]:

$$\lambda_{\text{de Broglie}} = \frac{h}{p} = \frac{h}{\sqrt{3m^* k_B T}} \tag{2.1}$$

where h is Planck's constant, p is carrier momentum, and k_B is Boltzmann's constant. The de Broglie wavelength for electrons in III-V semiconductor materials is in the order of 20 nm at 300 K. Several aspects of carrier confinement effects are useful for semiconductor device applications.

Figure 2.1 shows a schematic comparison between a bulk semiconductor, a waveguide for visible light, a QD, and an atom. The electronic structure of the bulk material and the atom are different. The electronic structure in the case of the atom is described by discrete energy levels, while in the case of the bulk-crystal structure we use band theory. Because the structural size is varied continuously, there exists a description between the two cases (discrete levels and continuum band structure). The densities of states of bulk semiconductor and low-dimensional nanostructures are illustrated in Figure 2.2 [26]. In confining direction, the band offsets between the low-dimensional nanostructures and the surrounding material provide the energy potential or potential well in energy band to confine the carriers. Therefore, the carrier motion is limited in this direction and allowed to move freely only in bulk dimension, which exist no potential well. Electrons and holes in a quantum well can freely move in the x-y plane; those in a quantum wire can only move in x direction. In a QD, zero-dimensional-nanostructure, the charge carriers are completely localized. This 3-D confinement results in a quantization of the carrier energy and in a variation of the carrier density of states.

The quantization phenomenon can be described by wave-like properties of electrons, since any substance would exhibit its wave properties of which de Broglie wave length can be calculated from eq. (2.1). In potential well, confined carriers are limited its motion, so they are looked-like stationary. The wave-like properties of the *stationary* electron can be only de Broglie wavelengths which create standing wave within the width of the potential well, that is, the width of the nanostructures. The discrete-values of electron de Broglie wavelengths would be exhibited, and cause discrete energy levels in such 3-D confinement structures. Schematic representation of the lowest three level of carrier's energy quantization appeared in potential well is shown in Figure 2.3.

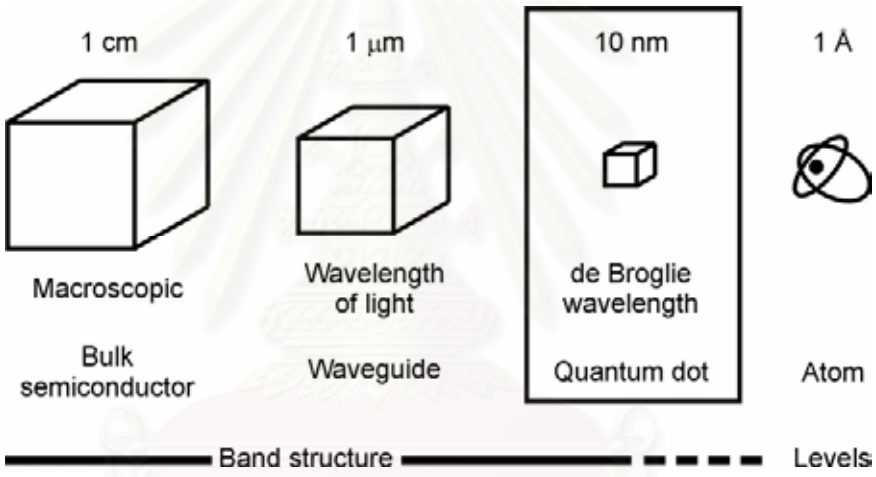

Figure 2.1 Schematic comparison of bulk semiconductor, waveguide for visible light, QD, and atom [27].

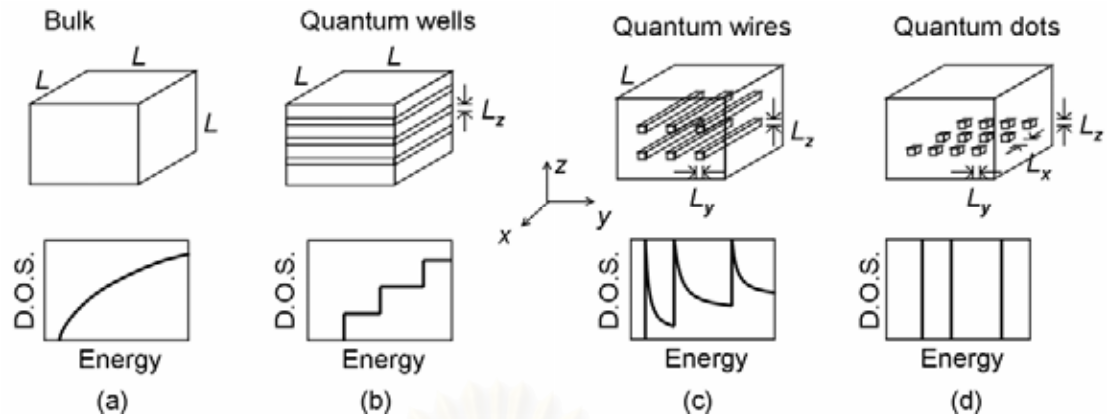

Figure 2.2 Schematic views and graphs of (a) bulk, (b) quantum wells, (c) quantum wires, and (d) QD and their density of states (D.O.S.) [26]. L is in macroscopic scale (~cm), while L_x, L_y, L_z, are in nanoscale.

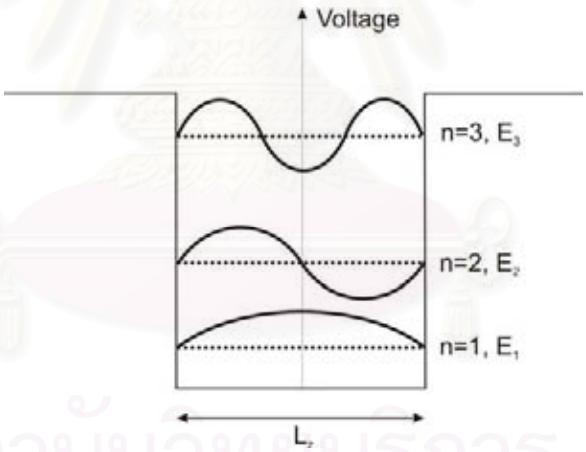

Figure 2.3 Schematic representation of the lowest three level of carrier's energy quantization in potential well with the width of L_z (comparable to de Broglie wavelength). The picture shows examples of the three lowest-energy standing waves which can be happened in potential well (solid line) and the corresponding carrier's energy level of the de Broglie wavelength from the standing wave (dotted line), i.e. E_1, E_2 and E_3. The energy of each level is given by $E_{n,z} = \eta^2 (n\pi)^2 / 2m^* L_z^2$, where n is a integer number of the level.

In semiconductor quantum wells, an effective-mass approximation is widely used for the quantized energy levels calculation as a function of the well width [28]. The main assumption of the effective-mass approximation is that the envelope wave function does not significantly vary in the unit cell with a length scale of subnanometers, therefore this assumption is valid in all low-dimensional nanostructures. Assuming parabolic band dispersion, band-edge electron states of semiconductors can be described by Schrödinger-like equation as

$$\left[-\frac{\eta^2}{2m^*}\nabla^2 + V(\mathbf{r})\right]F(\mathbf{r}) = E\,F(\mathbf{r}) \tag{2.2}$$

Here, m^* is the effective mass; $\hbar$ is the reduced Planck's constant; $\mathbf{r} = (x,y,z)$ is the carrier position vector; $V(\mathbf{r})$ is the confinement potential due to band offset. $F(\mathbf{r})$ is the envelope wave function; and E is the carrier energy.

From eq. (2.2), by assuming the barrier potentials with *infinite height*, the carrier energy E and density of states per unit volume (D.O.S.) (the number of states between the energy E and $E + dE$, of each quantum nanostructure) in case of bulk, quantum well (QW), quantum wire (QWR) and QD can be written as follow [26],

Bulk materials

$$E_{\text{bulk}} = E(\mathbf{k}) = \frac{\eta^2 k^2}{2m^*} \tag{2.3}$$

$$D_{\text{bulk}}(E) = \frac{1}{2\pi^2}\left(\frac{2m^*}{\eta^2}\right)^{3/2} E^{1/2} \tag{2.4}$$

where $\mathbf{k} = (k_x,k_y,k_z)$ is the wave vector of carriers and $k^2 = k_x^2 + k_y^2 + k_z^2$

Quantum well (QW)

Assuming that the confinement potential barrier for the square QW has infinite height, we obtain [26]

$$E_{\mathrm{QW}} = E(\mathbf{k}) = \frac{\eta^2 k_{//}^{\ 2}}{2m^*} + E_{n,z} = \frac{\eta^2}{2m^*}\left[k_{//}^{\ 2} + \left(\frac{n_z \pi}{L_z} \right)^2 \right] \tag{2.5}$$

$$D_{\mathrm{QW}}(E) = \frac{m^*}{\pi\, \eta^2 L_{QW}} \sum_{n_z} \Theta(E - E_{n_z}) \tag{2.6}$$

where $k_{//}^{\ 2} = k_x^2 + k_y^2$, Θ is the Heaviside's unit step function, n_z =1,2,3,…., and L_{QW} is the sum of the well and barrier regime thickness. From eq. 3.5, the minimum energy and the energy separation between each quantized state increase as the well width decreases.

Quantum wires

Assuming that the confinement potential barrier for the square QWires has infinite height, we get [26]

$$E_{\mathrm{QWR}} = E(\mathbf{k}) = \frac{\eta^2 k_{\perp}^{\ 2}}{2m^*} + E_{n_y} + E_{n_z} = \frac{\eta^2}{2m^*}\left[k_{\perp}^{\ 2} + \left(\frac{n_y \pi}{L_y} \right)^2 + \left(\frac{n_z \pi}{L_z} \right)^2 \right] \tag{2.7}$$

$$D_{\mathrm{QWR}}(E) = \frac{N_{wi}}{\pi} \frac{\sqrt{2m^*}}{\eta} \sum_{n_y,\, n_z} \frac{1}{\sqrt{E - E_{n_y} - E_{n_z}}} \tag{2.8}$$

where $k_{\perp}^{\ 2} = k_x^2$, n_y, n_z =1,2,3,…., and N_{wi} is the area density of the quantum wires (the number of quantum wires divided by the quantum-wire region area in the *y-z* plane).

Quantum dot

Assuming that the infinite confinement potential barrier in all direction, we get [26]

$$E_{\mathrm{QD}} = E_{n_x} + E_{n_y} + E_{n_z} = \frac{\eta^2}{2m^*}\left[\left(\frac{n_x\pi}{L_x}\right)^2 + \left(\frac{n_y\pi}{L_y}\right)^2 + \left(\frac{n_z\pi}{L_z}\right)^2\right] \tag{2.9}$$

$$D_{\mathrm{QD}}(E) = 2N_D \sum_{n_x,n_y,n_z} \delta(E - E_{n_x} - E_{n_y} - E_{n_z}) \tag{2.10}$$

where δ is the delta function, and N_D is the volume density of QD.

The change of density of states for the low-dimensional nanostructures (Figure 2.1) considerably affects the fundamental properties of the devices, which use these nanostructures as an active layer [29]. The electronic properties for QD structure differ drastically from the bulk system due to the discrete energy levels and delta peak density of states, which are in contrast to the continuous spectrum of the bulk. Hence QD structure sometimes was name as *artificial atom*. In case of QD structures, there are several theoretical and experimental proves that semiconductor lasers consisting of QD structures have the lowest threshold current density due to the delta-function-like density of states [30]. Figure 2.4 shows the historical evolution of the threshold current of semiconductor lasers [31].

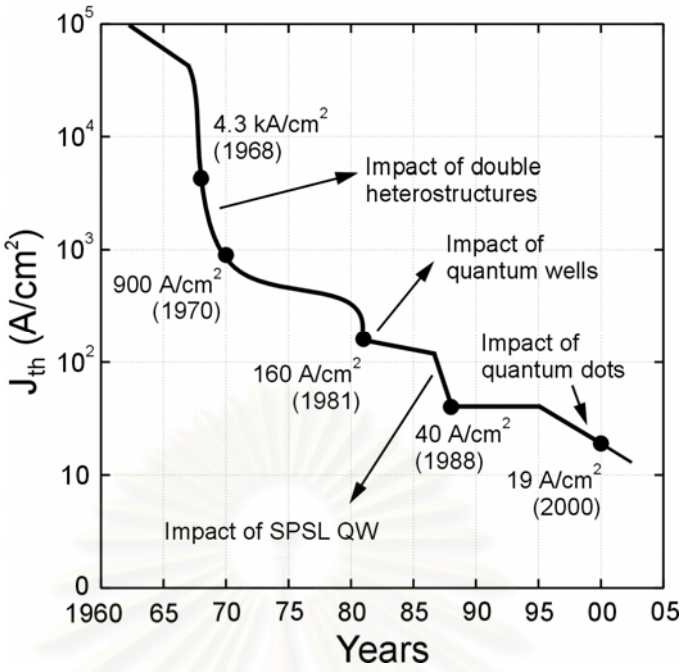

Figure 2.4 Evolution of the threshold current of semiconductor lasers [31].

To utilize QDs as an active layer for semiconductor lasers, there are two particularly important considerations. First, the density of QDs must be high enough to achieve the lasing condition (gain overcomes the loss). Second, the QD size distribution should be narrow since the optical gain spectra depend on the size distribution. In other words, QDs should have the same size in order to reduce the charge carriers needed for the population inversion condition. The maximum optical gain, g^{sat}, for a QD laser can be written as [32]

$$g^{sat} \propto N_e/\Delta \qquad (2.11)$$

where N_e is the number of states per unit surface. For the ground level, N_e is equal to the doubled surface density of the QD array, N_D. Δ is the total spectrum broadening from all excited QDs. From eq. (2.11), it is possible to increase the maximum optical gain by increasing the QD density and/or reducing the size distribution of the QD ensemble.

In summary, we introduced the concept of low-dimensional nanostructures, i.e. QWs, QWRs, and QDs compared with bulk semiconductors. The general theoretical view of the size and the electronic properties, i.e., density of states was presented.

2.1.2 Ring-shaped nanostructures

In this work, the Ring-shaped nanostructures, which can be classified as a type of quantum-confinement structure, have been observed. Like QDs, ring-shaped nanostructures have their energy level quantized so the certain-energy photon would be emitted when stimulated.

However, semiconductor quantum rings have attracted a great deal of attention because fascinating properties have been predicted and demonstrated [33, 34]. For example, the ring-structures are a special class of quantum-confinement due to the Aharonov-Bohm effect, which is a specific to the topology of a ring [35]. Another interesting is magnetic properties of quantum rings, which are related to the possibility of inducing persistent current.

The persistent current of a quantum ring [36] can be written in general as

$$I(\Phi) = -\frac{\partial F}{\partial \Phi}, \qquad (2.12)$$

where F is the free energy of system and Φ the magnetic flux piercing the ring. At zero temperature the free energy can be replaced with the ground state energy. The energy of the ring and consequently also the persistent current is a periodic function of the flux. The effect of the magnetic field is to lower the energy states of high angular momentum with respect of those at low angular momentum. When the flux is increased the ground state energy will jump from one angular momentum to the next causing the periodic behavior.

2.2 Self-assembled growth

The self-assembled growth, which can be realized a nanostructure such as QD, is presented in this section. The growth mode and growth conditions for self-assembled growth are briefly reviewed in order to provide some basic understanding of growth method. Droplet epitaxy is introduced since it is the fabrication technique which is used in this thesis work.

2.2.1 Growth modes

To define the growth mode which occur during the film deposition, we consider $\Delta\gamma$ which is the change of total energy of a surface before and after deposition:

$$\Delta\gamma = \gamma_F + \gamma_{S/F} - \gamma_S \tag{2.13}$$

where γ_S is substrate surface energy, γ_F is film surface energy, and $\gamma_{S/F}$ is interface energy between grown film and substrate which includes the additional energy arising from the strain between film and substrate.

If $\Delta\gamma > 0$, the deposited material would prefer to cover the substrate surface, then we obtain Frank Van der Merwe growth mode or layer-by-layer growth (Figure 2.5(a)). In this mode, the interaction between the substrate and deposited atoms is stronger than that between neighboring atoms. In the opposite case, if $\Delta\gamma < 0$, the 3D growth mode as Volmer Weber mode is observed (Figure 2.5(c)), where the interaction between substrate neighboring atoms exceeds the overlayer substrate interactions.

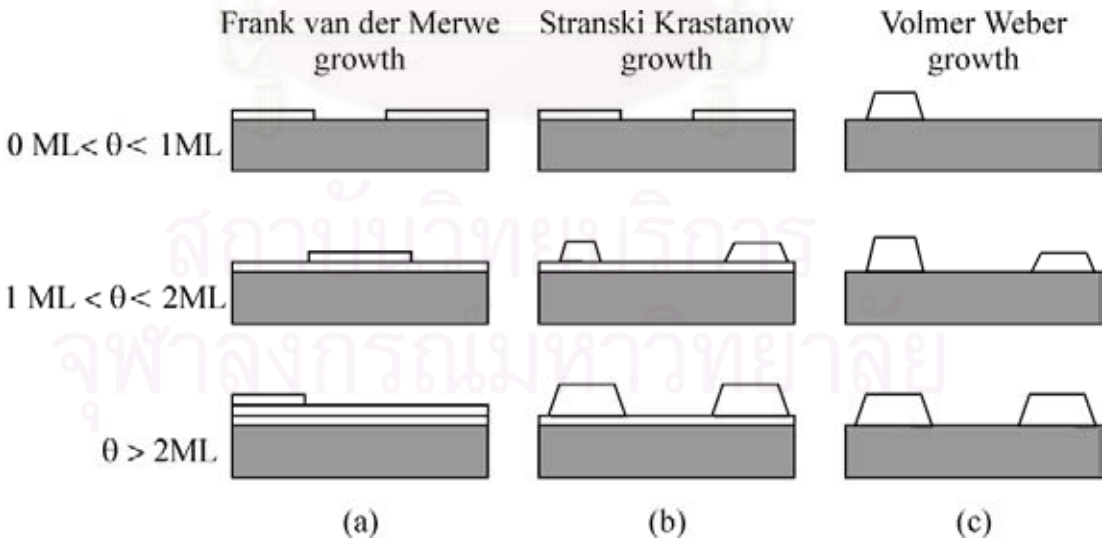

Figure 2.5 Schematic representation of the 3 important growth modes of a film for different coverage (θ) (a) Frank van der Merwe (FM); (b) Stranski Krastanow (SK) and; (c) Volmer Weber (VM) [37].

In an intermediate case, the deposited film can grow a few monolayers in layer-by-layer growth mode at the early stage of deposition ($\Delta\gamma < 0$). However, due to the strain between the grown film and substrate increasing with the deposited film thickness, the islands are formed on top of the *intermediate* layer, which is called the wetting layer (WL) since $\Delta\gamma$ becomes less than zero and growth mode changes from 2D-growth mode to 3D-growth mode. The case of layer-plus-island growth was named Stranski-Krastanow growth mode (Figure 2.5(b)).

2.2.2 Self-assembled growth in Stranski-Krastanow mode

Stranski-Krastanow (SK) growth mode is widely used to fabricate defect-free self-assembled QD structures in the case of lattice-mismatched system (lattice mismatch : ε_0 > 7%). In this section, although we have not used this method to fabricate the nanostructures in this work, the detail of SK growth mode is briefly introduced to provide the basic of QD formation from strain-releasing in lattice-mismatched system.

The illustration of the film growth in this growth mode is shown in Figure 2.6. First, a few monolayers of strained material grow in layer-by-layer growth mode. During the growth, elastic strain energy, E(el) builds up due to the lattice mismatch, given by [38]

$$E(\text{el}) = \lambda\, \varepsilon^2\, A\, t \qquad (2.14)$$

where λ is the elastic modulus, ε is the misfit, and A is surface area. The total energy for the layer-by-layer growth increases as a function of the film thickness t. Beyond the critical thickness, the layer-by-layer growth is unfavorable, and so elastic strain relaxation occurs. The local strain energy density of the SK-growth mode QD is schematically represented in Figure 2.7. The nanoscale islands formed in this mode can be used to confine carrier in three dimensions.

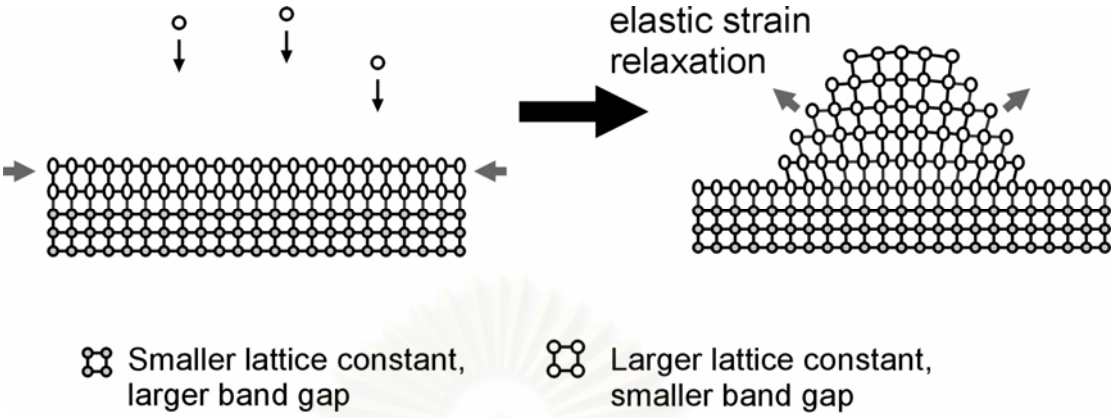

Figure 2.6 Illustration of island formation during epitaxial growth of a semiconductor material on top of another semiconductor with a smaller lattice constant in Stranski-Krastanow mode. The island formation is energetically favorable if we deposit material beyond critical thickness, because the lattice can elastically relax compressive strain and thus reducing strain energy.

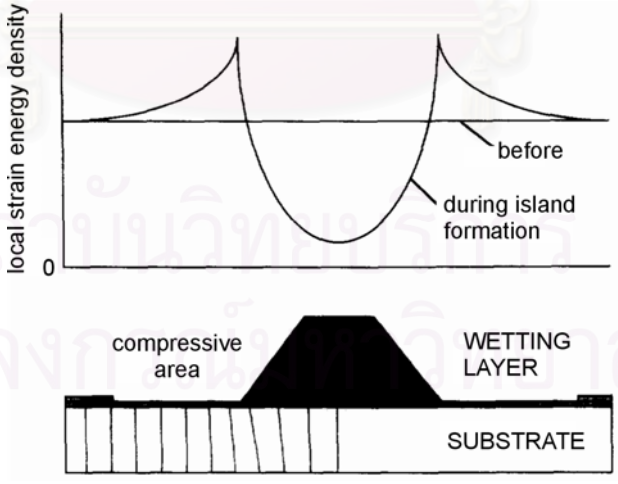

Figure 2.7 Schematic representation of the local strain energy density in and around the SK-growth mode QD. The energy barrier has a maximum at the edge of the QD [38].

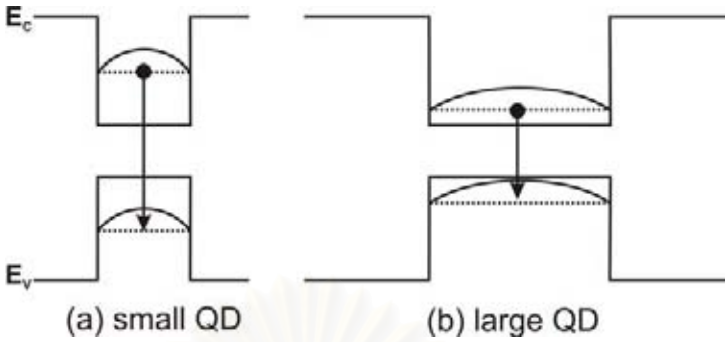

Figure 2.8 Simple interpretation of the energy level exhibited in the QD with different size. The representations in case of (a) small QD show the higher energy level than that of large QD (b) due to the carrier confinement properties. Electrons and holes in a small size QD would exhibit shorter de Broglie wavelength of which corresponding energy level is higher.

Although the QDs grown by this technique form into high-density arrays. There are still some disadvantages of this technique. First, the Stranski-Krastonow growth mode QDs exhibit wide size distribution which response to varying of energy level in the energy band. The representations of the energy level exhibited in the QD with different size are shown in Figure 2.8. Also, the non-uniform strain distribution from lattice-mismatched formation would effect on the band structure of QD [39]. Both are undesirable for laser applications.

2.2.3 Droplet epitaxy

From the viewpoint, well-defined strain-free nanostructures are desirable for studies of the physics of semiconductor ring structures. For the growth of high-quality self-assembled nanostructures in lattice-matched systems, droplet epitaxy is a promising method [1, 12, 15-17].

Droplet epitaxy is an alternative approach of self-organized nanostructure fabrication which can be applied to both lattice-matched and mismatched system. Unlike SK growth mode, the nanostructures fabricated by droplet epitaxy are

originated directly from strain-free group III-element droplets formed on III-V compound substrate instead of strain-releasing in lattice-mismatched system. The lattice-matched system in droplet formation would reduce the strain-energy in the nanostructure and its effects on the energy-band structure.

Droplet epitaxy process consists of 2 steps. The illustration of the nanostructure fabrication by droplet epitaxy is shown in Figure 2.9. First, group III-element droplets are formed on a III-V compound substrate by depositing group III-element on the substrate. The corresponding layer thickness of the droplet amount should be less than the critical thickness to prevent the formation of 3-D islands, which are QDs caused by strain-releasing from mismatch between the substrate and the overlayer in SK growth mode. Second, the group III-element droplets would be crystallized into III-V compound nanostructures by exposing them to group V-element molecular beam.

Since the droplets of group III-element are uniform, uniform-size III-V compound nanostructures can be formed by this method [1, 12, 15-17]. Furthermore, it is obvious that the shapes of the III-V compound nanostructures can be simply controlled by droplet forming parameters, such as, substrate temperatures and amount of group III-element deposited. Since the droplet properties are still metallic, their morphology can be varied by changing such parameters.

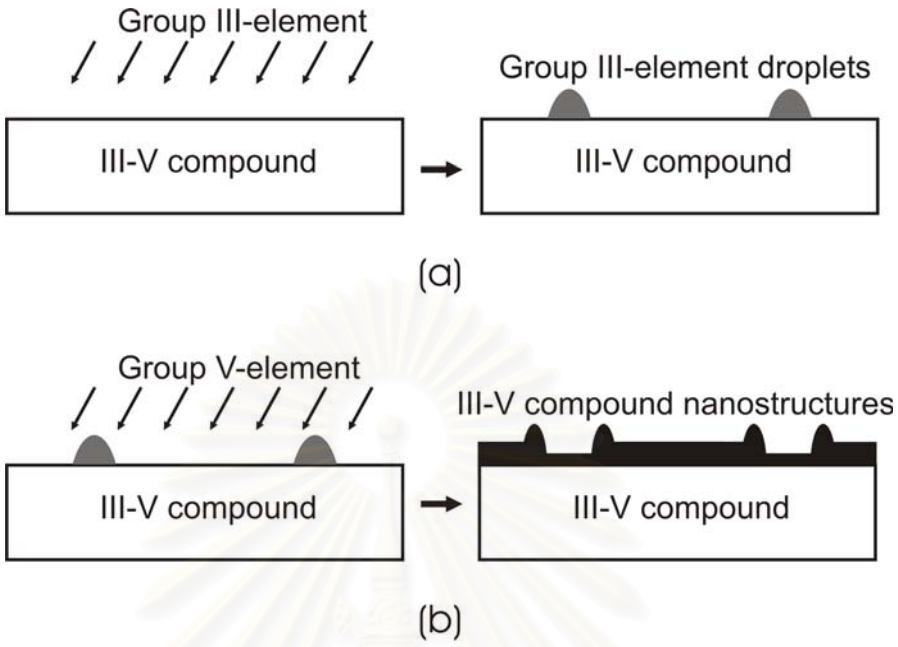

Figure 2.9 The illustration of the nanostructure fabricated by droplet epitaxy. First, (a) group III-element is deposited on a III-V compound substrate in order to form group III-element droplets. Then, (b) the group III-element droplets would be exposed to group V-element molecular beam in order to crystallize them into III-V compound nanostructures.

2.2.4 Material Considerations

Self-assembled growth can be carried out in several semiconductor material systems, e.g., In(Ga)As/GaAs, InP/InGaP, or SiGe/Si. The preliminary condition for the growth is that the nanostructure material has a smaller band gap compared with the substrate material to provide a potential well in energy band. The additional condition for SK growth mode is that the lattice constant of QD material must be larger than the one of substrate material (lattice mismatch : $\varepsilon_0 > 7\%$) to provide the lattice mismatch. On the other hand, the material for nanostructure fabricated by droplet epitaxy is not necessary to have the larger lattice constant since the method can be applied to lattice-matched system. Figure 2.10 shows the relationship between band gap energy and the lattice constant of III-As material systems.

For laser applications in optical communication systems, technologically, GaAs is the most important substrate material. The self-assembled growth of InGaAs on GaAs substrate can provide the nanostructures which emit light at 1.3 μm or longer wavelength depended on the ratio of In and Ga in the InGaAs structures . In this work, we will concentrate only on the InGaAs/GaAs material system.

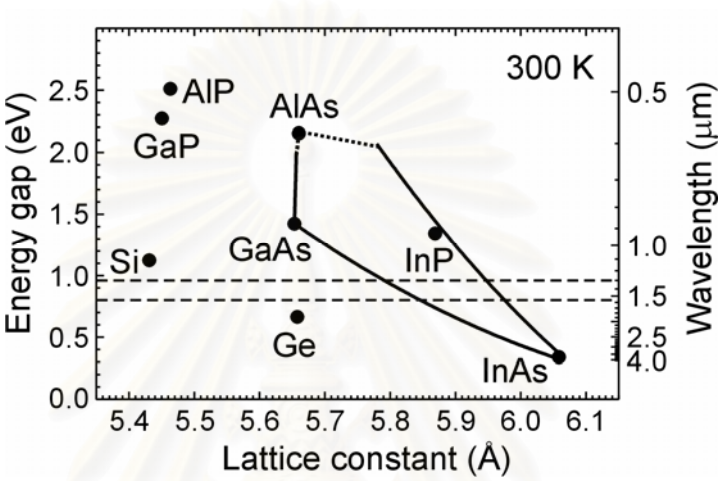

Figure 2.10 The relationship between lattice constant versus energy gap at room temperature for the III-As material system. The solid line is for direct band gap material and the dotted line is for indirect band gap material. From the figure we can see that there is a possibility to realize nanostructures which emit light at the wavelength of 1.3 μm or 1.55 μm (dashed lines).

CHAPTER III

EXPERIMENTAL DETAILS

The details of the sample fabrication by droplet epitaxy using molecular beam epitaxy (MBE) growth used in this work are explained in this chapter. The calibration of growth rate was done by in situ reflection high-electron energy diffraction (RHEED) observation. On the other hand, the samples were characterized by ex situ atomic force microscopy (AFM) and photoluminescence (PL) spectroscopy.

3.1 Molecular Beam Epitaxy (MBE)

Molecular beam epitaxy (MBE) was invented as a equipment for molecular design of material, exceptionally, as a popular technique for growing III-V compound semiconductors. With clean and ultra high vacuum (UHV) environment, the atomic or molecular beams of the constituent elements are incident upon a heated crystalline substrate. MBE provides several benefits. It can produce high-quality layers with very abrupt interfaces. In addition, it also has good control of thickness, doping, and composition, because of the precise control of beam fluxes and growth conditions. In the atomic structure, quantum effect is strongly found because the electron could show their virgin properties. This gives rise to quantum devices with high efficiency, high speed and high performance. It can be said that MBE structures closely approximate the idealized models used in solid state theory.

In this research, a conventional RIBER 32P MBE machine consisting of three UHV chambers, i.e., introduction chamber, transfer chamber, and growth chamber, is used to grow our samples. Three chambers are separated by isolation gate valves. Pumping system including sorption pump, ion pump, and titanium sublimation pump is installed to keep UHV condition. A figure of RIBER 32P MBE is shown in Figure 3.1. The pressure of each chamber is measured by ionization gauge. In case of growth chamber, there are two ionization gauges. One which is located at equivalent substrate position behind the substrate heater is used for measuring molecular beam flux and the other which is installed in front of the ion pump is used for measuring background

pressure. The substrate is rotated continuously while the epitaxial growth to provide uniform flux profile on substrate surface. The group III-elements, i.e., In, Ga and Al and group V-elements, i.e., As_4 are contained in pyrolytic boron nitride (PBN) crucibles which are installed in separated effusion cells. Each cell is heated by its own heater of which temperature is controlled by feedback from standard thermocouple via computer. The molecular beam flux of each constituent elements is controlled by tantalum shutter in front of each cell. A schematic drawing of the modified III-V MBE growth chamber is shown in Figure 3.2.

In sample preparation, the substrates need to be preheated by heaters in introduction chamber. A propose of preheat process is to eliminate contaminated substance, mainly water (H_2O), on substrate surface. After finish preheat process, the sample is transferred to the manipulator in growth chamber, preparing to start the fabrication.

The unique advantage of MBE from other techniques is that it enables to study and control the growth process in situ. In particular, reflection high energy electron diffraction (RHEED) allows directly measurement of surface structure of the sample and the already grown epilayer. The equipment of RHEED consists of a 20-kV electron gun, a fluorescent screen, a CCD camera, and a computer. In addition, the quadruple mass spectroscopy is also installed for particle analysis in growth chamber. The explanation on RHEED is presented in the next section.

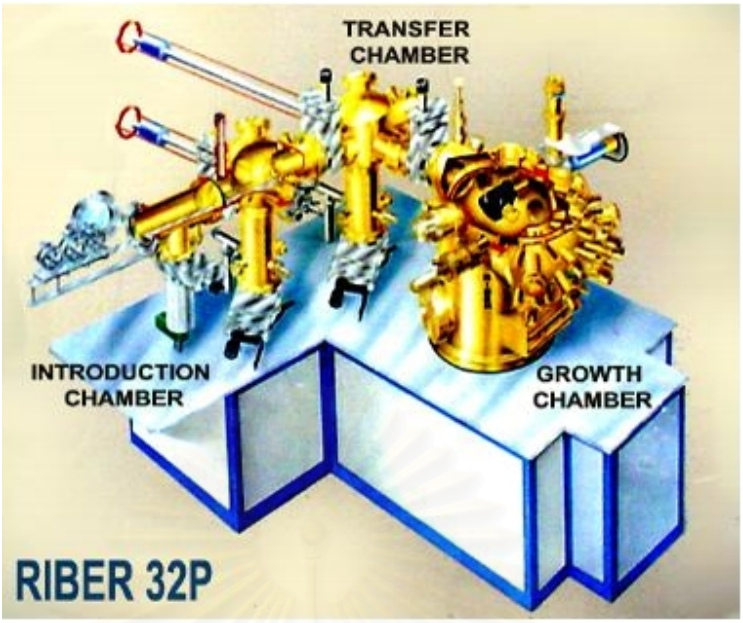

Figure 3.1 The conventional RIBER 32P MBE consists of three chambers, i.e., introduction chamber, transfer chamber, and growth chamber.

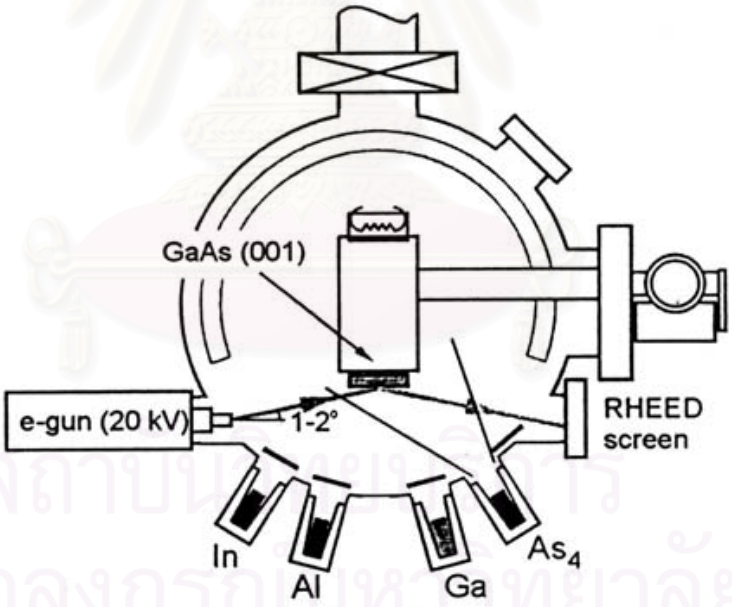

Figure 3.2 Schematic drawing of the modified III-V MBE growth chamber. The chamber is cooled by a closed circuit liquid N_2. The base pressure is less than 1×10^{-10} torr.

3.2 Reflection High Energy Electron Diffraction (RHEED)

Reflection high energy electron diffraction is an in situ equipment for characterizing thin films. It allows direct measurements of the surface structure of the sample and already grown epilayer. It also allows observation on the dynamics of MBE growth. The schematic representation of RHEED system is shown in Figure 3.3. An high-energy electron beam (~15 keV) intersects with the sample surface at a small angle (θ ~1-3^{o}). It is diffracted by the surface atoms, which function as grating. The scattering electrons interfere constructively and form a pattern on the fluorescent screen. The RHEED pattern would be captured with a high-performance CCD camera and analyzed with the sophisticated RHEED data processing software installed to the computer.

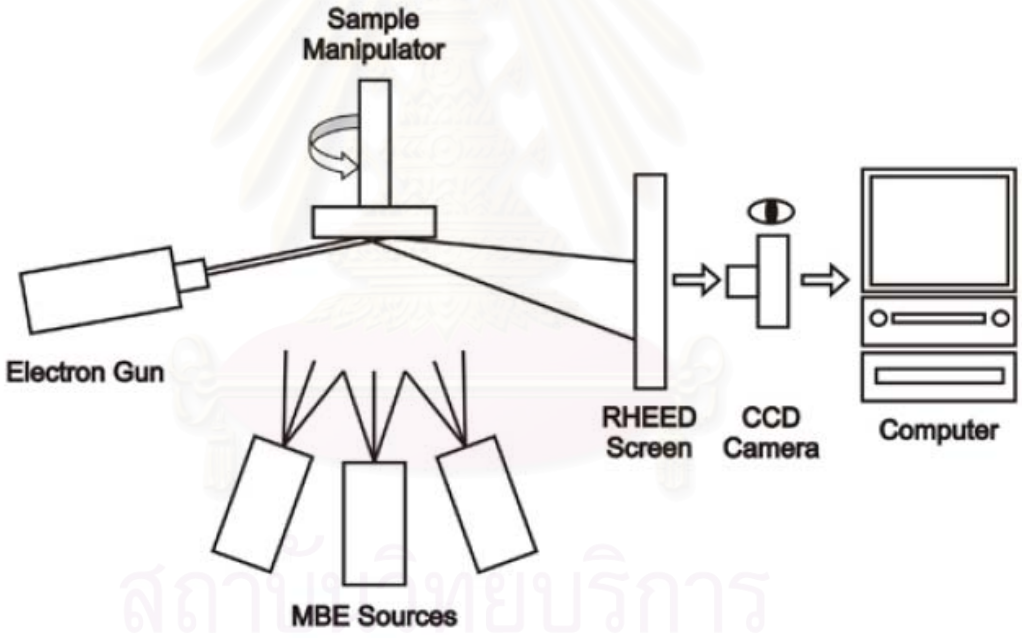

Figure 3.3 Schematic representation of RHEED system consisting of electron gun, fluorescent screen, high-performance CCD camera and computer with the sophisticated RHEED data processing software.

3.2.1 RHEED pattern observation

The pattern position can be graphically determined by the Laue method – intersection of Edwald sphere in reciprocal lattice space. The schematic representation of RHEED observation is illustrated in Figure 3.4. Since the short de Broglie wavelength of electron allows a shallow penetration depth into the substrate, the electron beam is restricted to the topmost atomic layers. Diffracted electron at the flat surface are imaged onto the screen. Therefore, the surface layer is represented by a reciprocal lattice space rod perpendicular to the real surface [37]. If the surface has roughness in the order of an atomic scale, the surface layer in the reciprocal space will be presented by three-dimensional point array. Therefore, we can interpret the RHEED pattern as the reciprocal lattice representation of the sample surface, which reflects the surface morphology on the atomic scale.

In this work, we use RHEED observation to monitor surface structure during the growth of GaAs buffer layer and during the growth of nanostructures.

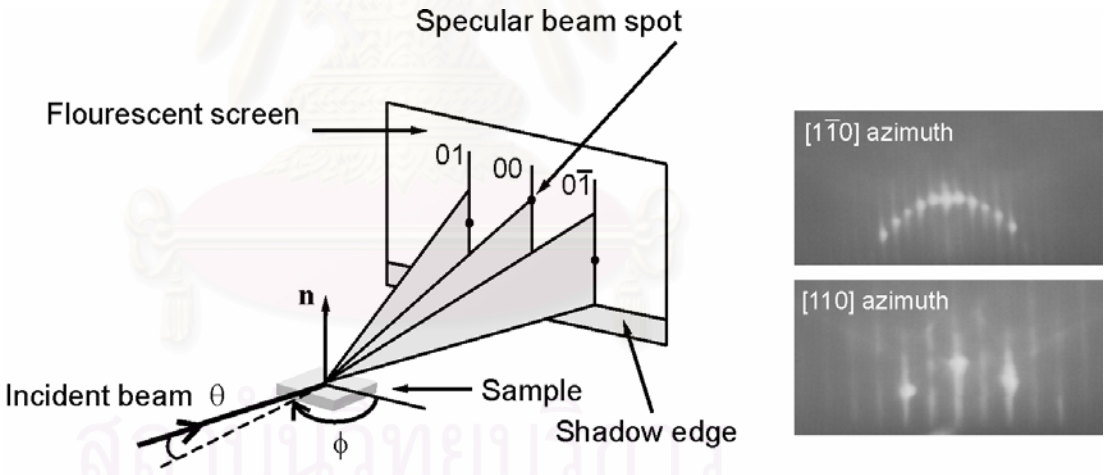

Figure 3.4 Schematic diagram of RHEED geometry showing the incident electron beam at an angle θ to the surface plane [37]. The right part shows diffraction pattern from the GaAs (001) (2×4) surface, in the [1-10] and [110] azimuths.

3.2.2 RHEED intensity oscillation

RHEED intensity oscillation can be used to determine the growth rates. This has been also used to calibrate beam fluxes corresponding to the growth rate. To control alloy composition and the thickness of quantum structures grown, the fluxes are adjusted to the value corresponding to needed growth rate [37].

The RHEED intensity on the pattern depends on the roughness of the surface. Under the normal growth condition, the RHEED intensity, i.e., surface roughness, changes according to the fraction of surface coverage where the period of the pattern oscillation corresponds to the growth of 1 monolayer (ML). The schematic representation of the RHEED intensity oscillation is shown in Figure 3.5. In each period, the maximum reflectivity occurs at the initial and final state when smooth surface was completely grown and minimum reflectivity occurs at the intermediate state when the growing layer is approximately half completed. With use of the period of oscillation signal, the growth rate of GaAs can be calibrated. The experimental data is shown in Figure 3.6.

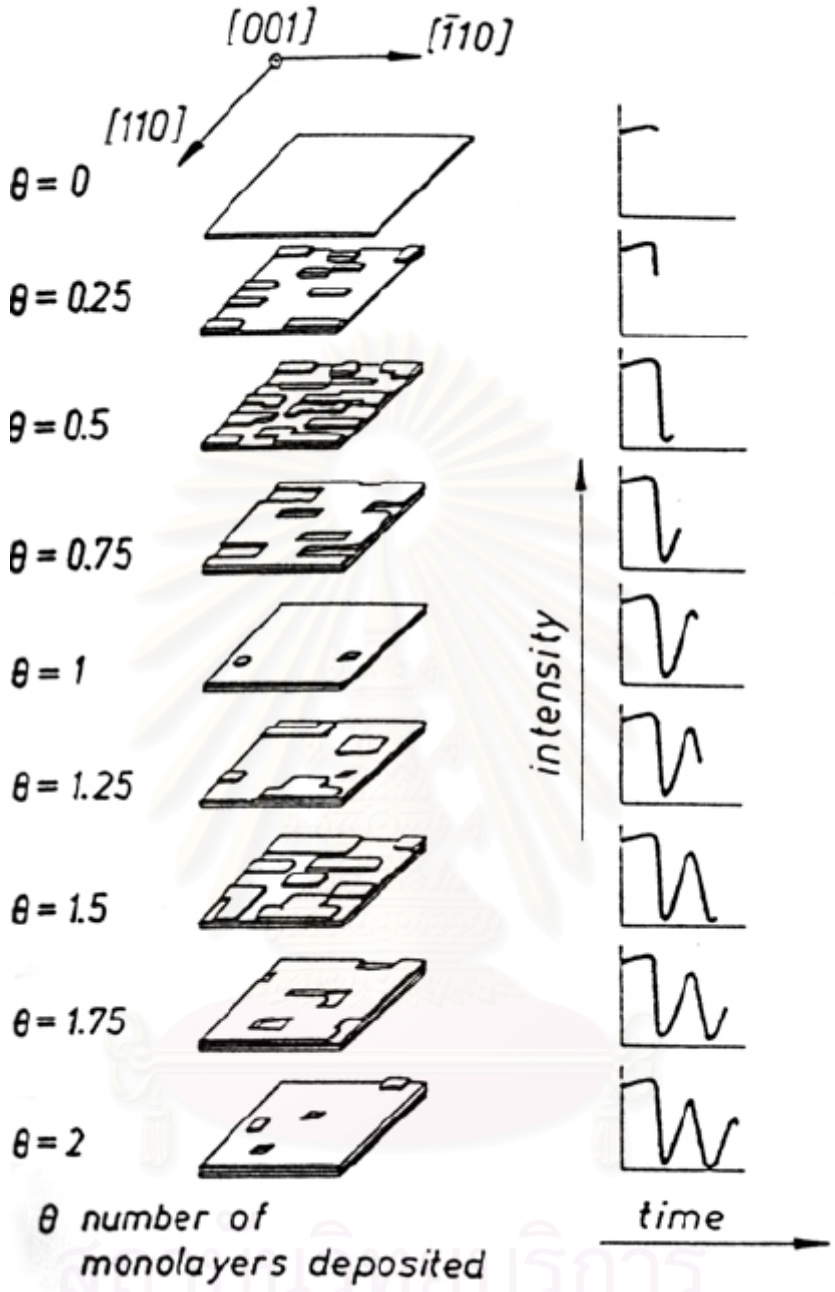

Figure 3.5 Schematic representation of RHEED intensity oscillations related to formation of the first two complete monolayer of GaAs (001) [37].

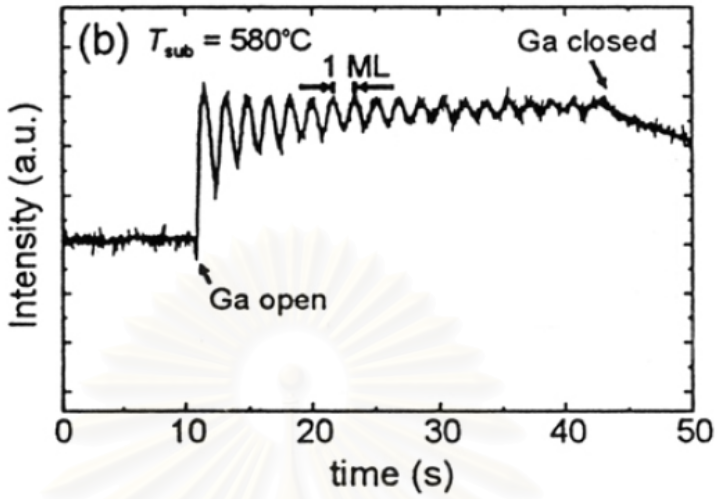

Figure 3.6 RHEED intensity oscillation obtained during the growth of GaAs.

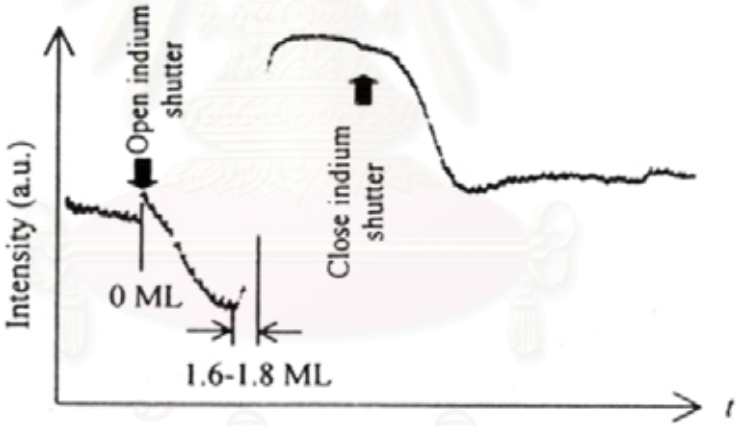

Figure 3.7 The intensity of RHEED oscillation in case of InAs.

3.3 Atomic Force Microscopy (AFM)

The atomic force microscope (AFM) is a very powerful microscope invented by Binnig, Quate and Gerber in 1986. The schematic representation of AFM system is shown in Figure 3.8. The AFM consists of a cantilever with a sharp tip at its end, typically composed of silicon or silicon nitride with the size in the order of nanometers. The tip is brought into close proximity of a sample surface. The schematic representation of AFM measuring modes are shown in Figure 3.9. Typically, the deflection is measured using a laser spot reflected from the top of the cantilever into an array of photodiodes.

In this work, the AFM images are performed by using SEIKO SPA 400-AFM. The AFM is operated in the tapping mode in order to reduce the friction during the measurement. The scan rate is about 1-2 Hz and the scan size is usually $2\times2\ \mu m^2$ with 512 data points per scan line. So the lateral resolution is about 4 nm (2000 nm/512 data points).

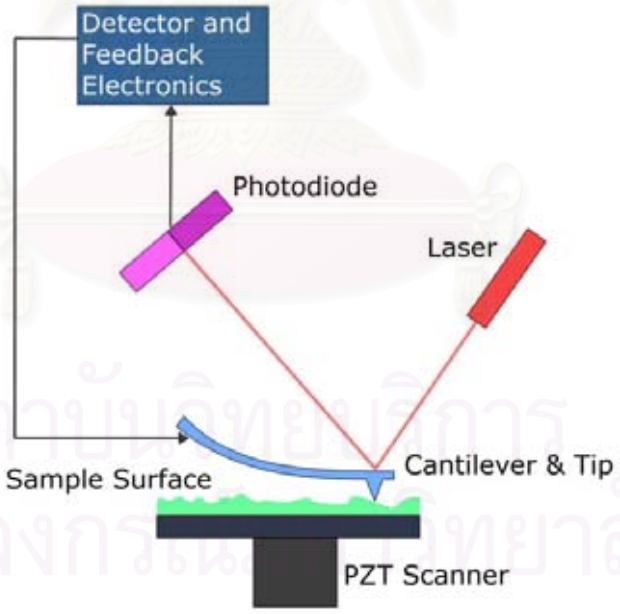

Figure 3.8 Schematic drawing of Atomic Force Microscopy (Drawn October 12, 2002 by Allen Timothy Chang)

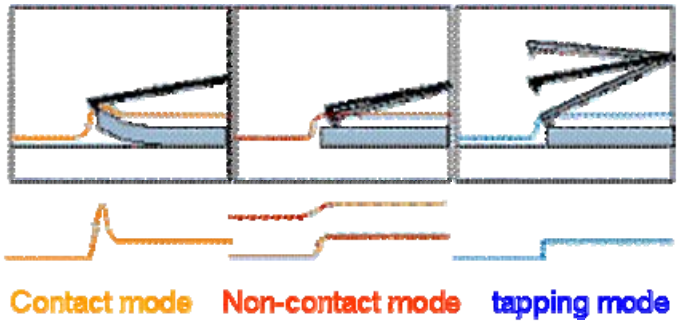

Figure 3.9 The schematic representation of AFM measuring modes including contact mode, non-contact mode and tapping mode. In this work, the AFM is operated in the tapping mode to reduce the friction when measuring.

3.4 Photoluminescence (PL) spectroscopy

Photoluminescence (PL) spectroscopy is a tool for sample luminescence characterization in this work. The samples were excited by the 488-nm line of an Ar+ laser. A schematic of the PL experimental setup is shown in Figure 3.10. The laser beam was chopped focused to the sample by focal lens. The light signal is analyzed by monochromator with photomultiplier tube. A high-pass filter is used to filter the visible-light noise and the reflected laser beam signal. Then, the resolved light is detected by a InGaAs detector. A chopper and the lock-in amplifier are used to enhance the signal by the standard lock-in technique.

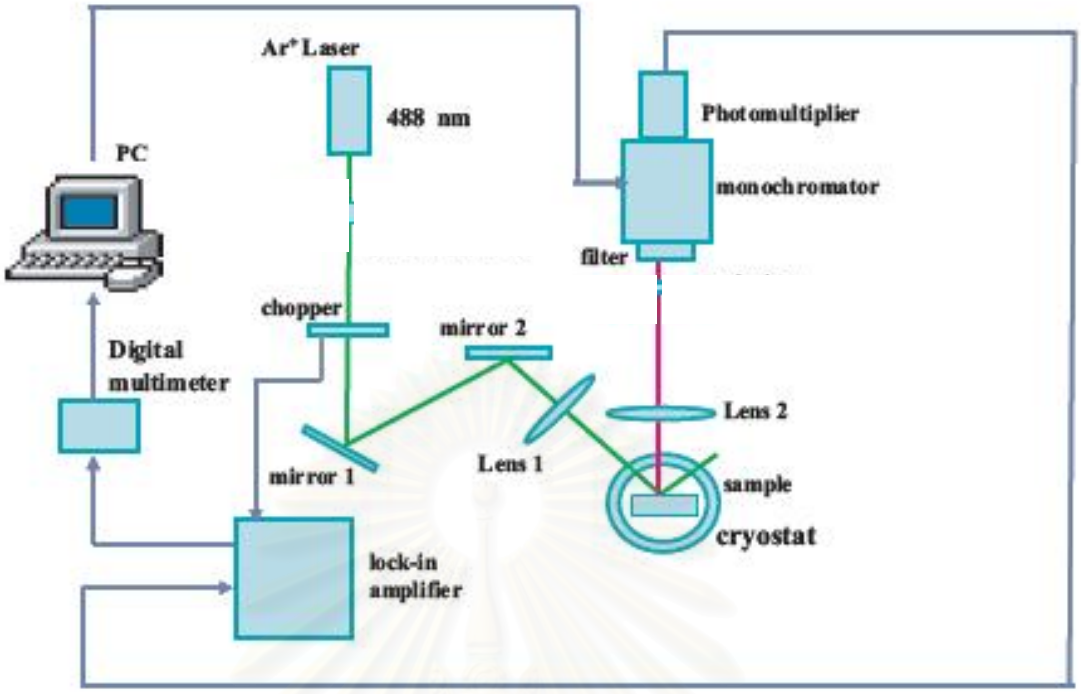

Figure 3.10 Schematic of the PL experimental setup

The interpretation of PL data can simply be described as shown in Figure 3.11 and Figure 3.12. For the case of nanostructures with different size in Figure 3.11, the ground state PL peak energy contains information about the size of the nanosturcture. The increase in nanostructure size results in a lower number of quantized energy levels of both holes and electrons, which causes a lower PL peak energy position. Therefore, this PL peak position can be used to relatively compare the size of nanostructure.

For the shape of PL spectrum from nanostructure array (Figure 3.12), there exists broadening of the spectrum. This broadening, which is measured in terms of a full width at half maximum (FWHM) or PL linewidth, is related to the nanostructure size distribution.

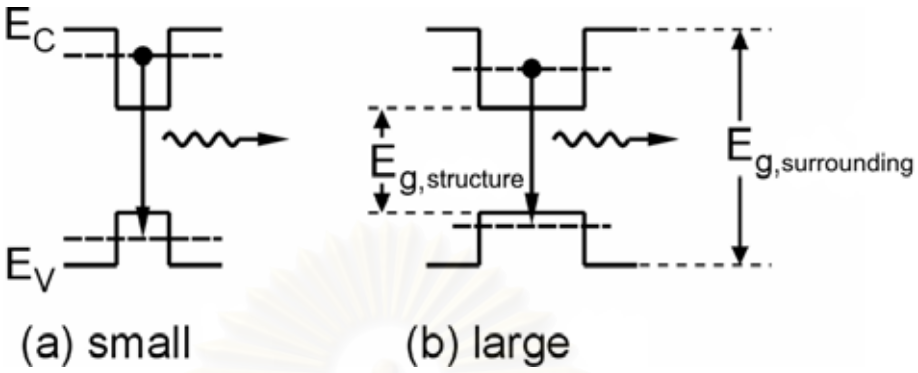

Figure 3.11 Simple interpretation of the PL data obtained from a nanostructure. In case of small-size nanostructure (a) the PL peak energy position is higher compared with large-size nanostructure (b).

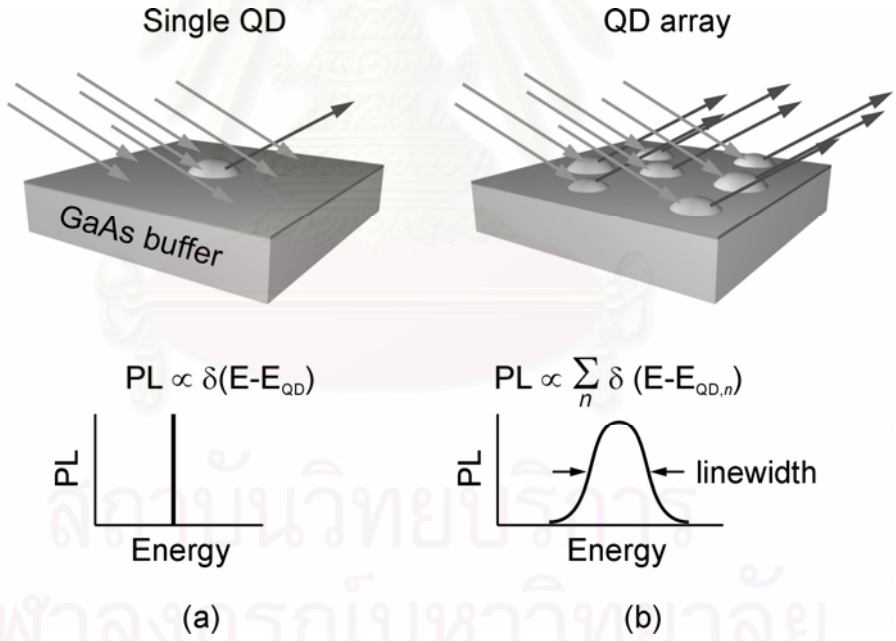

Figure 3.12 Simple interpretation of the PL spectrum obtained from the nanostructure. In (a) the PL spectrum is very narrow due to the delta-function like density of states; and in (b) the *average size* corresponds to the PL *peak* energy position and the PL *linewidth* corresponds to the *size distribution* of the array.

3.6 Sample preparation

In this work, the samples of InGaAs nanostructures were fabricated by droplet epitaxy using RIBER 32P molecular-beam epitaxy-system on GaAs (001) substrates. The growth conditions of the nanostructure have been varied in step of droplet formation. The detailed sequences for sample preparation are as follows.

(1) Pre-heated : A piece of epi-ready semi-insulating (001) GaAs substrate is glued on a Mo (molybdenum) block by using indium glue. The block with the substrate is transferred to the introduction chamber and heated to 450^{o}C for 60 minutes in order to eliminate water (H_2O) and oxide from the substrate.

(2) Deoxidation (removing oxide from substrate surface) : After preheated, the sample (the substrate on Mo block) is transferred into the growth chamber. Then, the substrate temperature is increased to 600^{o}C under As_4 pressure of ~ 7×10^{-6} torr until the streak RHEED pattern appeared in order to remove the native oxide from the surface. Streak RHEED pattern is shown in Figure 3.13.

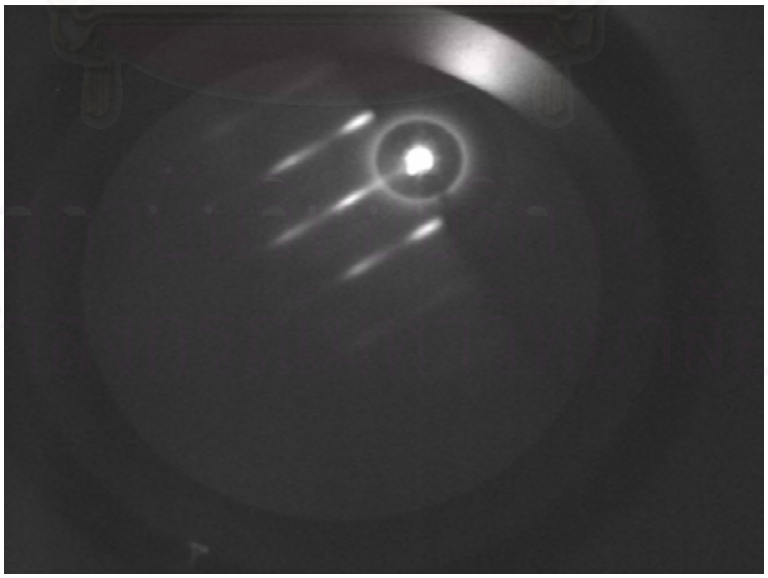

Figure 3.13 Streak RHEED pattern observed during the de-oxidation process.

(3) Growth of GaAs buffer layer : After the oxide removal at 600^{o}C, the substrate temperature was decreased and a 300-nm thick GaAs buffer layer was grown at 580^{o}C to flatten the surface. The GaAs growth rate is ~ 1 monolayer/s (ML/s). The sharp and clear streaky (2×4) RHEED pattern is always observed after finishing the growth of buffer layer. Streaky (2×4) RHEED pattern of GaAs surface is shown in Figure 3.14.

(4) Formation of InGa droplets : The growth conditions have been varied in this step. First, the substrate temperature was decreased to 530 ^{o}C without As_4 beam flux and hold for 10 minutes in order to eliminate exceeded As atoms from the surface. Then, the substrate temperature was reduced again to varied temperatures of 120, 150, 180 and 210^{o}C without As_4 flux (the background pressure was kept below 2×10^{-9} torr). Subsequently, a different amount of $In_{0.5}Ga_{0.5}$ corresponding to layer thickness 2, 3, 4 and 5 ML was deposited on GaAs buffer layer with deposite rate of 1 ML/s in order to form InGa droplets. The RHEED pattern of rings observed after annealing in As_4 is shown in Figure 3.15. (Note that $In_{0.5}Ga_{0.5}$ amount corresponding to thickness 4 and 5 ML was deposited only on 150^{o}C substrate.)

(5) Crystallization : Finally, the InGa droplets were crystallized into InGaAs by supply of As_4 flux ($6\text{-}7\times10^{-6}$ torr beam equivalent pressure (BEP)) at 180^{o}C substrate and annealed under As_4 flux supply for 5 minutes. For AFM measurement, the substrate temperature was decreased to 100^{o}C and loaded out of the growth chamber, and MBE system. The Mo block with the sample would be heated and the sample was separated from the block for AFM measurement. The schematic diagram of sample structure after crystallization was illustrated in Figure 3.16 (a).

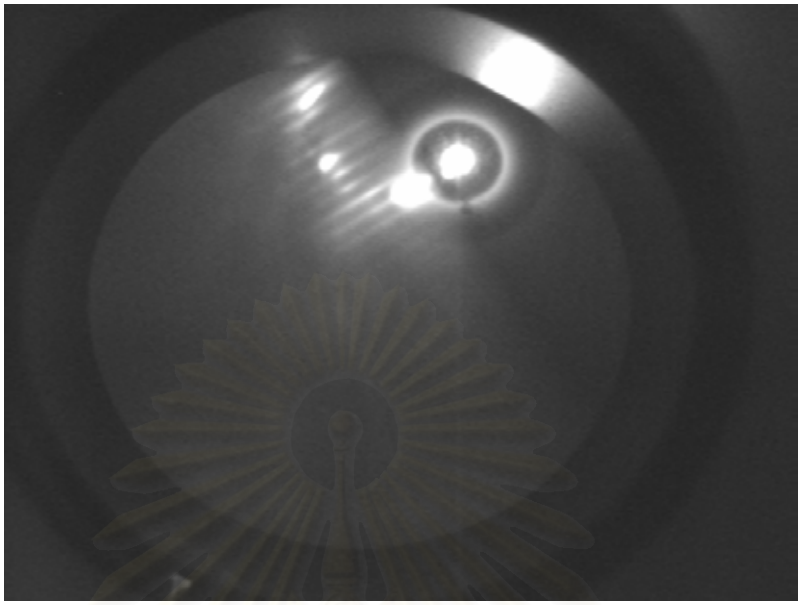

Figure 3.14 Streaky (2×4) RHEED pattern of GaAs surface observed after the formation of GaAs buffer layer.

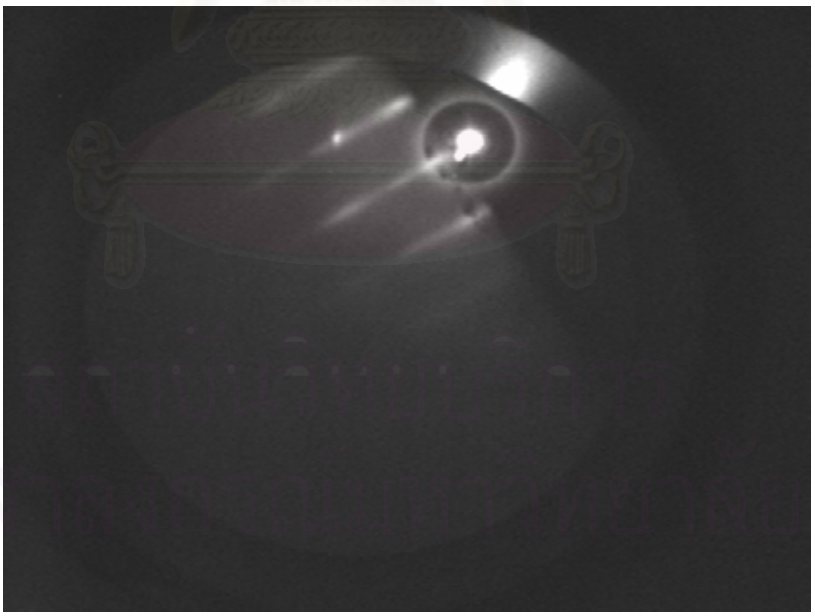

Figure 3.15 The RHEED pattern of ring structures observed after crystallized under As_4 flux.

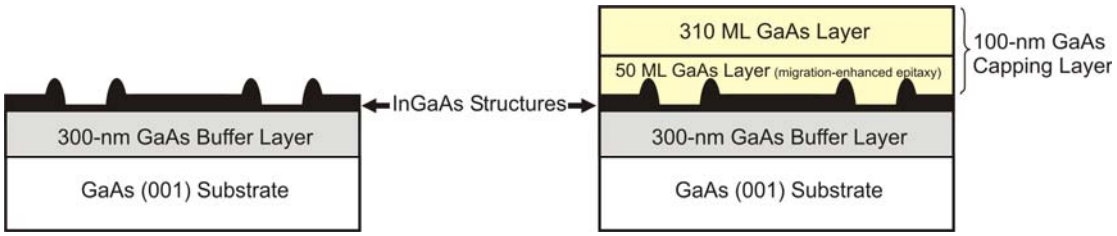

(a) (b)

Figure 3.16 Schematic diagram of the sample structures grown in this work (a) after crystallization in As_4, and (b) after capped with 100-nm GaAs capping layers. The details of growth sequences and growth conditions for the InGaAs nanostructures were given in the text.

(6) GaAs Capping : For PL measurement, another sample under the droplet forming condition of 3 ML InGa deposition at 210°C substrate was grown repeatedly with additional 100-nm GaAs capping layers. To grow the capping layers, after the entire growth sequences (1-5), the substrate temperature was slowly increased to 350°C with 5 minutes annealing in As_4 flux for each step of 250°C, 300°C and 350°C. Then, the capping layers were grown, including 50 ML of GaAs grown by migration-enhanced epitaxy (alternatively deposite Ga 2 seconds (0.5ML/second), As 2 seconds and anneal 2 seconds for 50 cycles) [21, 22] at 350°C and 310 ML of conventional-GaAs layers grown at 400°C respectively. The schematic diagram of sample structure after capped with 100-nm GaAs capping layers was illustrated in Figure 3.16 (b).

CHAPTER IV

RESULT AND DISCUSSION

In this chapter, the experimental results of InGaAs nanostructures grown by droplet epitaxy are shown. The ring-shaped InGaAs nanostructures have been observed. We have varied the droplet forming parameter, including amount of InGa deposited and substrate temperature while depositing droplets. By using atomic force microscopy (AFM), the effects of each droplet forming parameter on the size and density of the nanostructures can be investigated. Finally, the nanostructures have been re-fabricated under selected droplet forming condition with additional GaAs capping layers for photoluminescence (PL) measurement. The analytical optical properties of the InGaAs rings have been investigated from PL spectra of capped InGaAs-ring sample at 77 K.

4.1 InGaAs ring-shaped nanostructures : surface morphology

For structural characterization, the surface morphology of the samples after crystallization under As_4 flux (sequence (5) in section 3.6) was investigated by tapping-mode atomic force microscope (AFM) in air. The low density ring-shaped InGaAs nanostructures have been observed. At each droplet forming condition, the ring structures are mostly found to be uniform. However, at different droplet forming conditions, the nanostructure size and density are found to be different related to droplet forming parameters, i.e., substrate temperature and amount of indium (In) and Gallium (Ga) deposited. The AFM images of the sample surfaces after crystallization with size and density of InGaAs ring-shaped nanostructures are shown in Figure 4.1. The effects of each parameter are discussed in next sections.

The appearance of InGaAs ring-structures can be simply described. The formation mechanism of InGaAs ring-shaped nanostructures form metallic InGa droplets are roughly compared to the expansion mechanism of typical liquid droplets. The process is illustrated schematically in Figure 4.2. First, liquid-phase metallic InGa droplets are formed after the deposition of In and Ga on the GaAs substrate. Like

liquid droplets, the down-hill transport causes the diffusion of In and Ga atoms in the droplets. It results in two-dimensional expansion of the droplets. At the moment, some As atoms at the topmost of GaAs buffer layer can interact with InGa atoms in the droplets especially at the edge of the droplets. Hence, InGaAs are formed at this area, causing not-fully-crystallized InGa hemispherical-shaped structures [40]. Second, during the crystallization under As_4 flux, the rest InGa atoms from the droplets would diffuse to As atoms deposited on nearby surface (supplied from the flux) [41] and crystallized into InGaAs. Efficient crystallization is expected at the edge of the droplets [40, 41]. As a result, ring-shaped structures of epitaxial InGaAs are formed surrounding the droplet positions [40]. Figure 4.3 show the surface morphology and cross-sectional structure of a ring after annealing in As_4 flux in the case of InGa 3 ML and substrate temperature 210°C.

In next section, the dependence of the size and the density of InGaAs ring-shaped nanostructures on the substrate temperature and deposited InGa amount are discussed in detail.

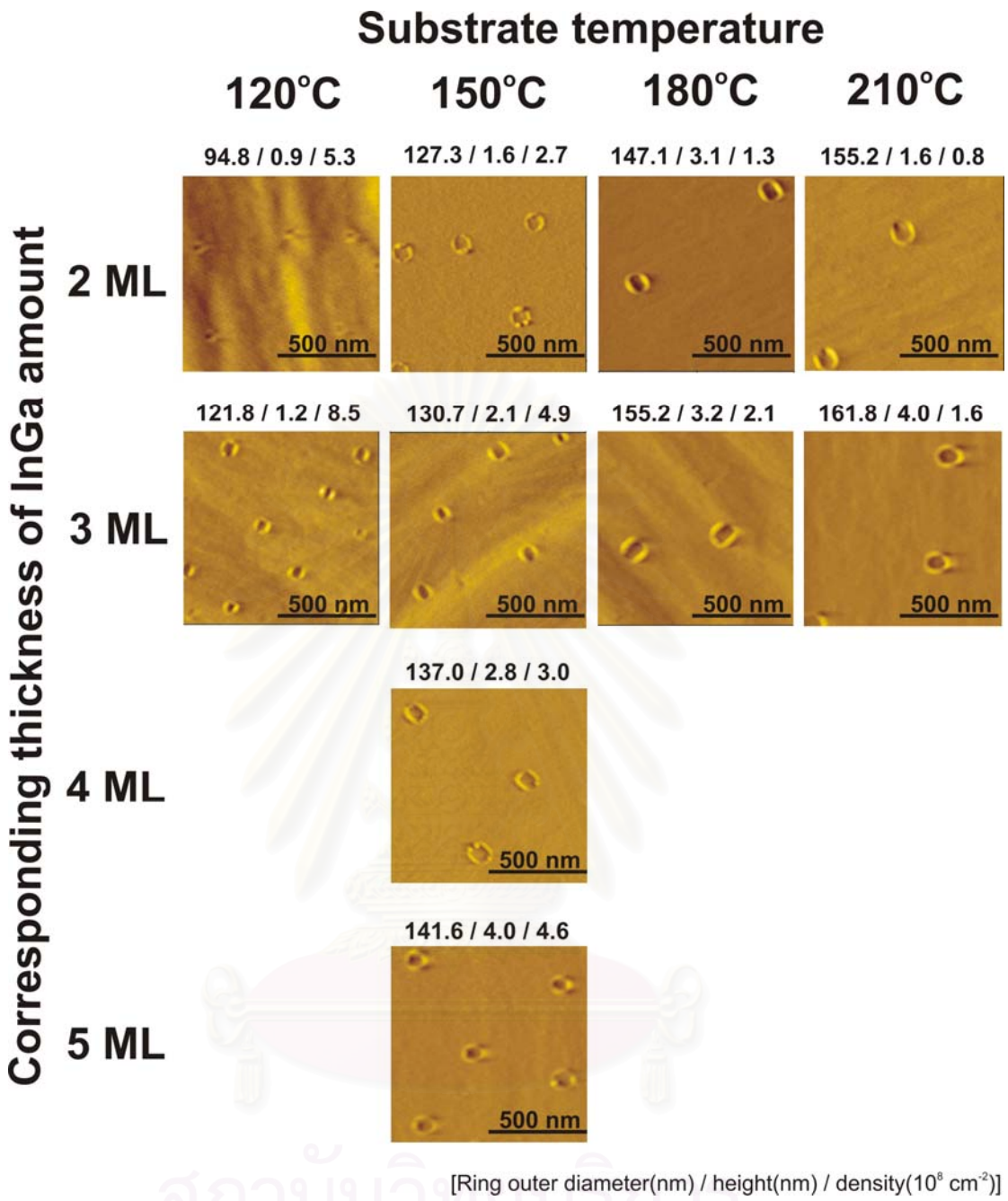

Figure 4.1 The 1×1 μm^2 AFM images of the surface morphology of the samples fabricated under different droplet forming conditions, including substrate temperature 120, 150, 180, 210°C and InGa amount corresponding to layer thickness 2, 3, 4, 5 ML. The low density ring-shaped InGaAs nanostructures have been observed. Above each images, the outer diameter (nm), height (nm) and density (10^8 cm^{-2}) of the InGaAs rings fabricated under each droplet forming condition are shown respectively.

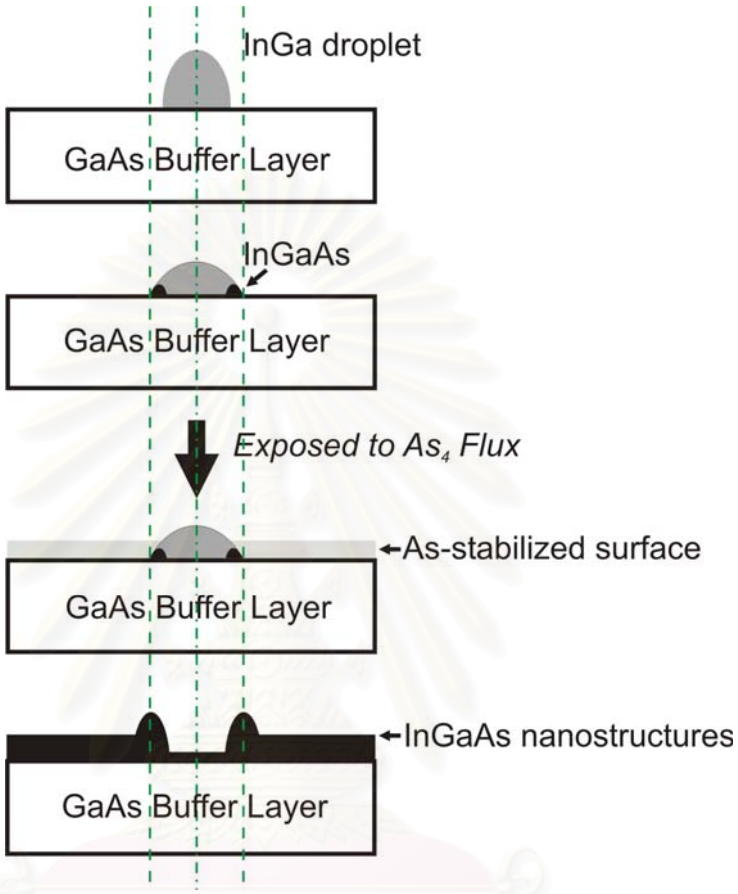

Figure 4.2 The formation mechanism of InGaAs ring-shaped nanostructures from metallic InGa droplets. First, the InGa droplets would expand in 2-dimensional direction because of the down-hill transport. At the moment, the edge of expanding InGa droplets can interact with As atoms at topmost of GaAs buffer layer and form InGaAs. Next, during the crystallization under As_4 flux, InGa atoms from the droplets would diffuse to As atoms on nearby surface and crystallized into InGaAs.

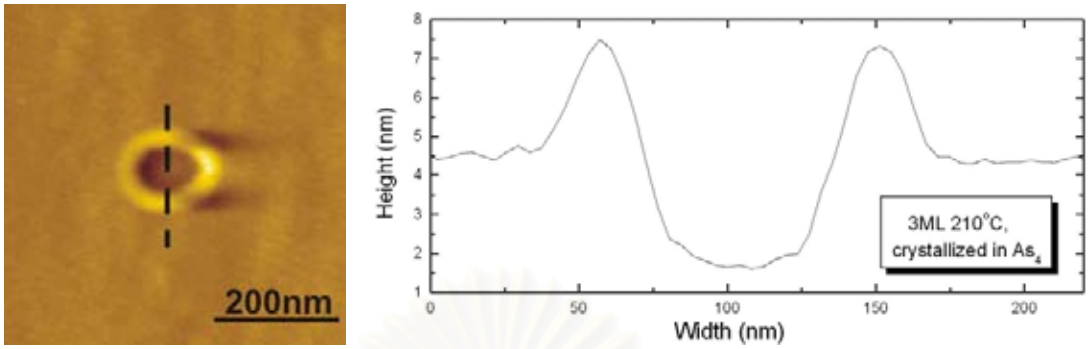

Figure 4.3 The 0.5×0.5 μm^2 AFM image and cross-sectional structure (along the dash line) of an InGaAs ring after annealing in As_4 in the case of InGa amount corresponding to 3 ML and substrate temperature 210°C.

4.1.1 Effect of substrate temperature on InGaAs ring-shaped nanostructures

To analyze the effects of substrate temperature while depositing droplets on InGaAs ring-shaped nanostructures, we have characterized the surface morphology of the samples in the series of InGa amount corresponding to 2 and 3 ML with 120°C - 210°C substrate temperature. The dependence of the ring-shaped nanostructure diameters and heights on the substrate temperature are shown in Figure 4.4 (a) and Figure 4.4 (b) respectively. Also, the dependence of the ring-shaped nanostructure density on the substrate temperature is shown in Figure 4.5. From the images, when increasing the substrate temperature, the ring size is increased but the density is decreased. The ring size includes the typical outer diameter and the height of the ring-structures along [001]. For example, under a condition of 3 ML $In_{0.5}Ga_{0.5}$, the density was 8.5×10^8 nm^{-2} with the ring outer diameter of 121 nm and height of 1.2 nm when the substrate temperature was 120°C, and the density was decreased to 1.2×10^8 cm^{-2} with the outer diameter of 161.8 nm and height of 4.0 nm when the substrate temperature was 210°C.

For explanation, greater size of InGaAs ring structures was caused from two-dimensional expansion of InGa droplets at high temperature. Migration of the InGa atoms in the droplets response to this expansion. Since, the diffusion (migration)

length of metallic In and Ga atoms in the droplets is proportional to the temperature of the substrate which they are deposited on. As a result, when substrate temperature is higher, greater diffusion length of metallic In and Ga atoms would response to wider 2-dimensional expansion of InGa droplets. After crystallization, the larger diameter of InGaAs ring-shaped nanostructures can be observed. On the other hand, the diffusion ability also results in the coalescence (mergence) of neighbouring metallic InGa droplets. Hence, at higher substrate temperature, the coalescence of InGa droplets would be more, resulting in greater quantity of InGa in each droplet. The droplets were also expected to be higher. After crystallizing such droplets, fewer but larger and higher InGaAs ring-shaped nanostructures would be observed.

For 2 ML InGa droplet forming condition, we have found that the heights of InGaAs rings turned to decrease at 180°C– 210°C substrate. It can be supposed that when wider expansion of InGa droplets occurred, the heights of such droplets had reached their limitation due to the limit of InGa amount deposited. Thus, wider but low InGaAs rings would be formed after finishing crystallization.

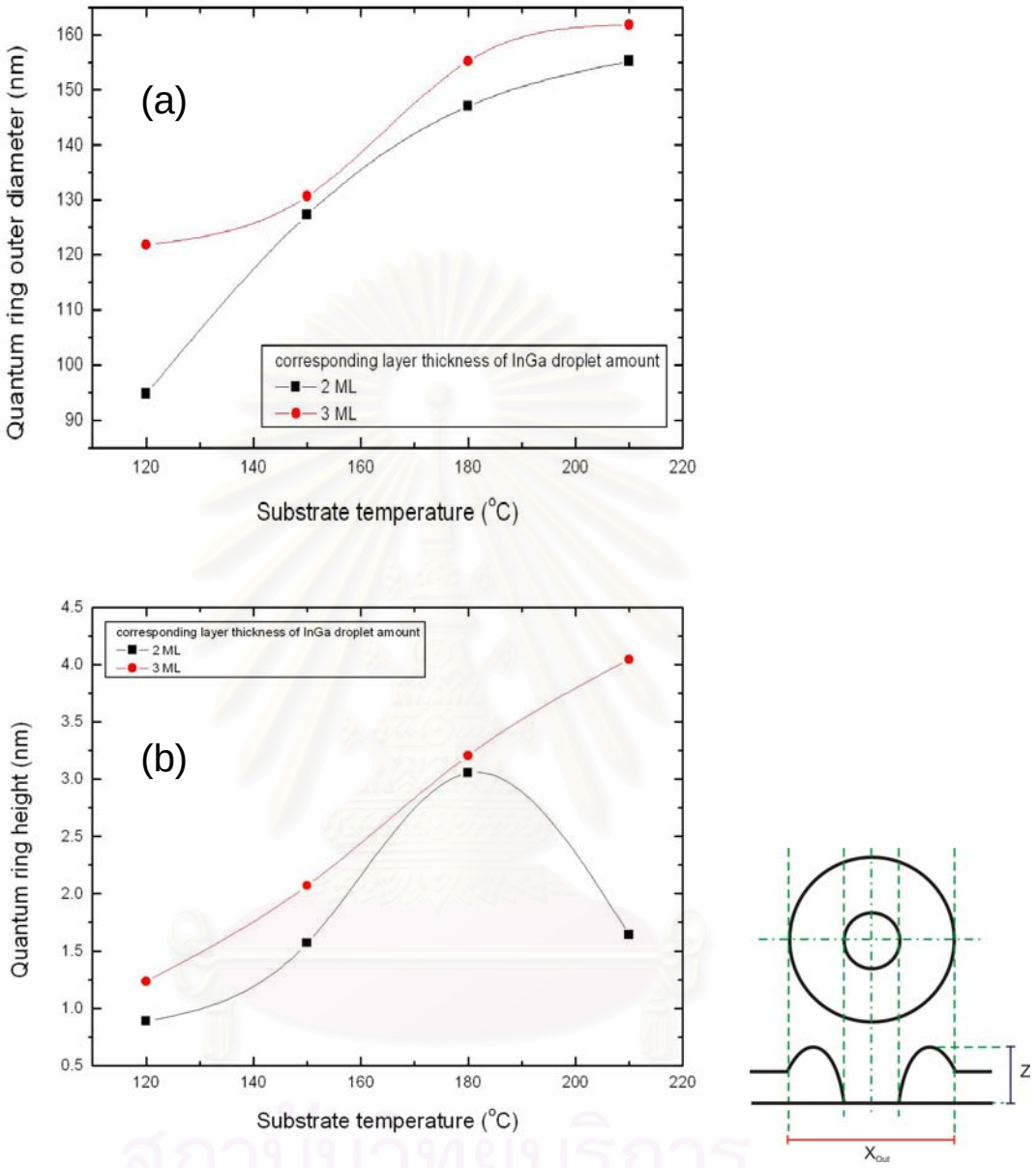

Figure 4.4 The dependence on the substrate temperature of ring-shaped nanostructure size including (a) the outer diameters (X_{Out}) and (b) the heights (Z) of the ring-structures.

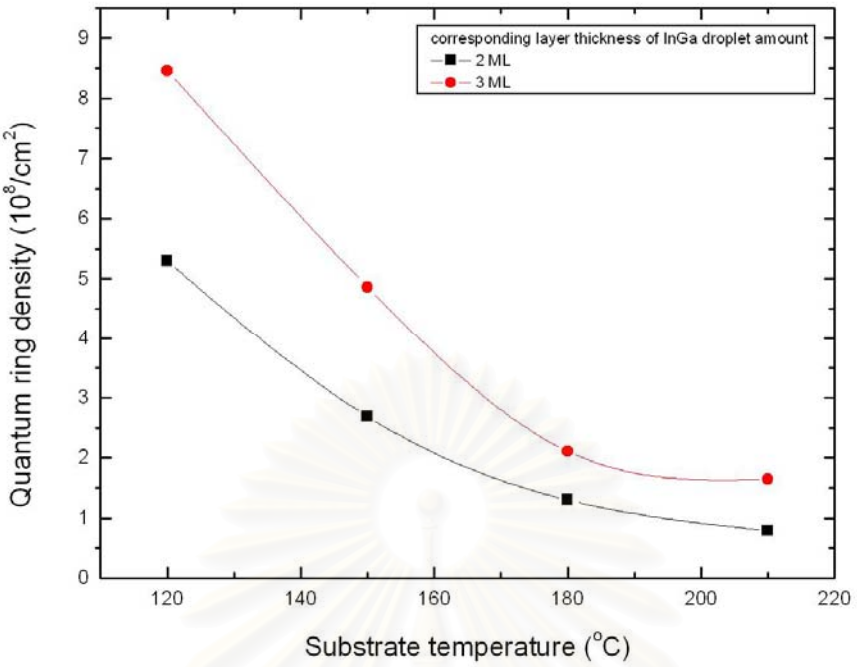

Figure 4.5 The dependence of the ring-shaped nanostructure density on the substrate temperature.

4.1.2 Effect of InGa amount on InGaAs ring-shaped nanostructures

To analyze the effects of deposited InGa amount on InGaAs ring-shaped nanostructures, we have characterized the surface morphology of the samples in the series of 150°C substrate temperature with InGa amount corresponding to 2, 3, 4 and 5 ML (from Figure 4.1). The dependence of the ring-shaped nanostructure diameters and heights on the InGa amount are shown in Figure 4.6 (a) and Figure 4.6 (b), respectively. Also, The dependence of the ring-shaped nanostructure density on the InGa amount is shown in Figure 4.7. From the images, it was found that increasing InGa amount deposited would result in the rings larger size, including the diameter and height. The density is also increased, when increasing InGa amount between 2-3 ML. However, when keeping InGa amount increased to 4 ML, the density turns to decrease. The density is increased again when increasing InGa amount to 5 ML.

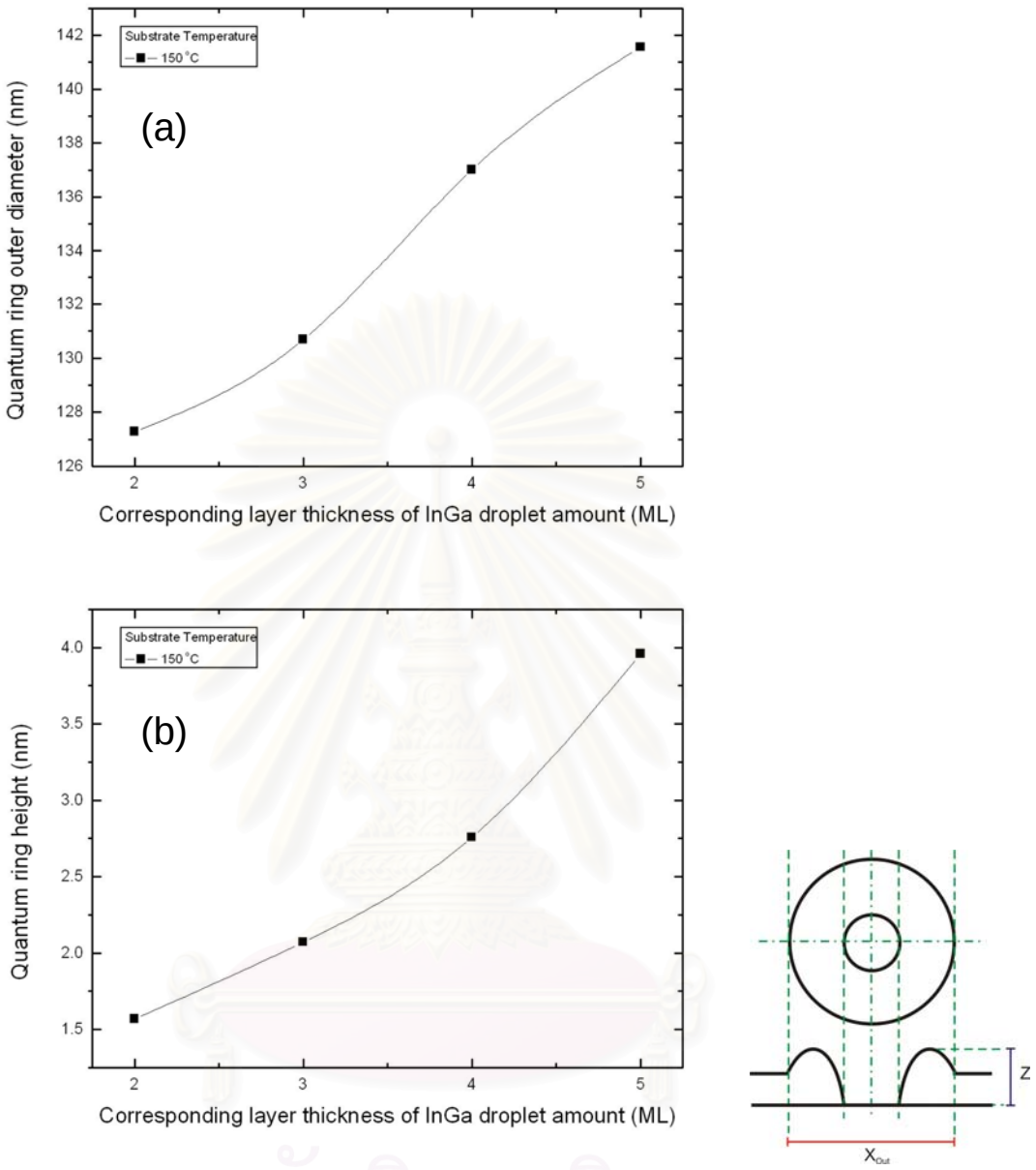

Figure 4.6 The dependence on the InGa amount deposited of ring-shaped nanostructure size including (a) the outer diameters (X_{Out}) and (b) the heights (Z) of the ring-structures.

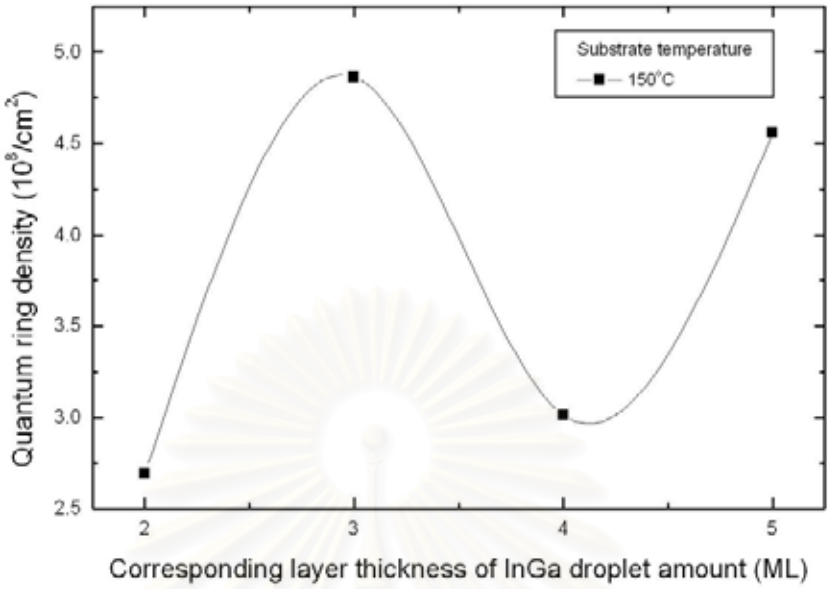

Figure 4.7 The dependence of the ring-shaped nanostructure density on the InGa amount.

The supposition of decreasing density when increasing InGa amount can be described. The Schematic drawing is illustrated in Figure 4.8. First, greater amount of InGa deposited would be enough to form full-layer of metallic InGa beyond the surface instead of individual droplets. Since deposited InGa atoms still exhibit their metallic properties, the neighbouring metallic InGa droplets tend to partially merge together. Thus, if there are enough metallic droplets covering the surface, it was supposed that full-layer of metallic InGa should be formed instead of individual InGa droplets. Subsequently, when following InGa adatoms were deposited, additional droplets would be formed above the layer, resulting in *renewal* of number of the droplets formed, as found in 4 and 5 ML InGa conditions.

By the way, a few smaller-size quantum rings were observed at 4 and 5 ML InGa condition. The ratio of the number of small rings to the normal size rings is about 1:6. We supposed that the small ring-structures were caused from strain in the nanostructures due to the increase of InGa layer thickness. Since InGaAs nanostructures with additional InGaAs layers below (from InGa full-layers) were formed after crystallized, strain-energy in the structures was increasing. The strain would compress the structures of InGaAs formed.

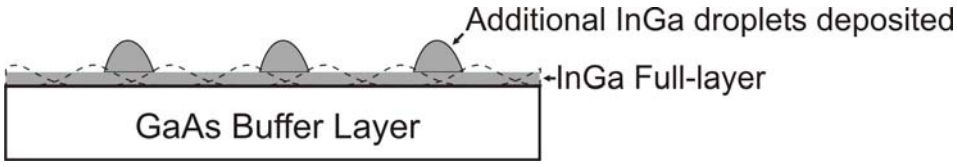

Figure 4.8 The Schematic drawing of a InGa full-layer with additional InGa droplets formed above when greater amount of InGa were deposited. It was supposed to result in renewal of the droplet density. First, the previous-layer droplets (dash line) have been coalesced and formed InGa full-layer instead. When newly supplied InGa adatoms were deposited, additional InGa droplets would be formed above the layer. Hence, the density of the droplets has been renewed.

4.2 Photoluminescence (PL) measurement of InGaAs ring-shaped nanostructures

For photoluminescence (PL) measurement, another sample under droplet forming condition of 3 ML InGa at 210°C substrate was grown repeatedly with additional 100-nm GaAs capping layers including 50 ML of GaAs layers grown by migration-enhanced epitaxy at 350°C and 310 ML of conventional GaAs layers grown at 400°C, respectively. The analytical optical properties of the InGaAs rings are confirmed by the photoluminescence spectra of the respective samples at 77 K. Ar^+ ion laser light at 488 nm was used as an excitation source and data were obtained by means of a cooled InGaAs photodetector in a spectrometer. Figure 4.9 shows the measured PL spectrum of the capped InGaAs-ring sample measured at 77 K. PL emission from the capped InGaAs ring-structures is centered at 950 nm (1.30 eV) with respective PL Full Width Half Maximum (FWHM) of 50 nm. PL lines around 840 nm stem from GaAs bulk. However, the PL intensity was found to be low due to low density of the ring structures existed.

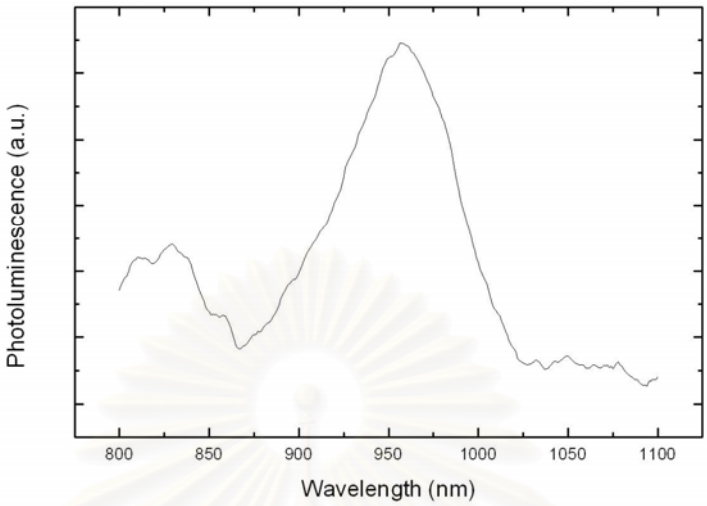

Figure 4.9 The photoluminescence (PL) spectrum at 77 K of the InGaAs ring-structures (fabricated under droplet forming condition of 3 ML InGa at 210°C substrates) with 50 ML GaAs-capping layers by migration-enhanced epitaxy at 350°C, and 310 ML of conventional GaAs layers grown at 400°C, respectively. The PL peak and respective FWHM are shown.

CHAPTER V

CONCLUSIONS

This work presents the growth of InGaAs ring-shaped nanostructures by droplet epitaxy using molecular beam epitaxy (MBE). By varying droplet forming conditions, the effects of droplet forming parameters including substrate temperature and InGa amount deposited on the InGaAs ring-structures were studied.

First, a brief overview on the properties of low-dimensional nanostructures was given, including quantum rings, or the ring-shaped nanostructures. As example of the QD fabrication in lattice-mismatched system, self-assembled growth in the Stranski-Krastanow mode was briefly reviewed. Details of droplet epitaxy that was the lattice-matched method used to fabricated the nanostructures in this work were given. From material considerations, the information of the material system including InGaAs/GaAs was discussed.

In situ RHEED observations were used to determine the growth rates and monitor surface structures during the growth of GaAs buffer layers and during the growth of nanostructures. The surface morphology and structural properties of the samples with InGaAs ring-shaped nanostructures were investigated by *ex situ* atomic force microscope (AFM) and photoluminescence (PL) measurement at 77 K.

The fabrication of InGaAs ring-shaped nanostructures was done by droplet epitaxy technique using solid source molecular beam epitaxy (MBE). The growth sequences included 6 steps : 1) pre-heated, 2) deoxidation, 3) growth of GaAs buffer layer, 4) formation of InGa droplets, 5)crystallization to InGaAs and 6) GaAs capping (only for PL measurement). InGa droplet forming conditions have been varied in order to investigate the effect of substrate temperature during InGa deposition and deposited amount of indium (In) and Gallium (Ga) on InGaAs ring-structures.

After crystallization (step(5)), the surface morphology of the samples were characterized by tapping-mode AFM. The low density ring-shaped InGaAs nanostructures have been observed. It was found that increasing substrate temperature during InGa deposition resulted in InGaAs rings larger size but lower density. It was suggested that greater diffusion length of metallic In and Ga atoms responsed to 2-

dimensional expansion of InGa droplets and coalescence of neighbouring droplets. As a result, after crystallization such droplets, larger but fewer InGaAs rings would be formed. Also, increasing InGa amount deposited would result in InGaAs rings larger size. The ring density is also increased when increasing InGa amount between 2-3 ML. However, when keeping InGa amount increased to 4 ML, the density turns to decrease. The density is increased again when increasing InGa amount to 5 ML. It was supposed that decrease of ring density was caused from formation of InGa full-layer instead of individual droplets when greater amount of InGa was deposited. Subsequently, newly supplied InGa adatoms would form the droplets above the layer resulting in renewal of the number of the droplet formed.

For PL measurement, the InGaAs ring-structures were repeatedly grown under selected droplet forming condition with additional 100-nm GaAs capping layers. The capping layers included 50 ML of GaAs layers grown by migration-enhanced epitaxy at 350°C and 310 ML of conventional GaAs layers grown at 400°C, respectively. The analytical optical properties of the InGaAs rings are confirmed by the PL spectra of the GaAs-capped InGaAs ring-structures at 77 K. PL emission from InGaAs ring structures is centered at 950 nm with respective full width at half maximum (FWHM) of 50 nm. PL lines around 840 nm stem from GaAs bulk. However, the PL intensity was found to be low resulting from low density of the ring structures existed.

REFERENCES

[1] N. Koguchi, S. Takahashi, and T. Chikyow. J. Crystal Growth 111 (1991): 688.

[2] D. Leonard, M. Krishnamurthy, C.M. Reaves, S.P. Denbaars, and P.M. Petroff. Appl. Phys. Lett. 63 (1993): 3203.

[3] R. Nötzel, J. Temmyo, and T. Tamamura. Nature 369 (1994): 131.

[4] M. Bayers, M. Korkusinski, P. Hawrylak, T. Gutbrod, M. Michel, and A. Forchel. Phys. Rev. Lett. 90 (2003): 186801.

[5] E. Ribeiro, A.O. Govorov, W. Carvalho Jr., and G. Medeiros Ribeiro. Phys. Rev. Lett. 92 (2004): 126402.

[6] Y. Aharonov, and D. Bohm. Phys. Rev. 115 (1959): 485.

[7] K. Nishi, T. Anan, A. Gomyo, S. Kohmoto, and S. Sugou. Appl. Phys. Lett. 70 (1997): 3579.

[8] V. Bressler-Hill, S. Varma, A. Lorke, B.Z. Nosho, P.M. Petroff, and W.H. Weinberg. Phys Rev. Lett. 74 (1995): 3209

[9] A. Lorke, R. J. Luyken, J. M. Garcia, and P. M. Petoff. Jpn. J. Appl. Part 1 40 (2001): 1857.

[10] N. P. Kobayashi, T. R. Ramachandran, P. Chen, and A. Madhukar. Appl. Phys. Lett. 68 (1996): 3299.

[11] Y. Nabetani, T. Ishikawa, S. noda, and A. Sasaki. J. Appl. Phys. 76 (1994): 347.

[12] N. Kokuchi, and K. Ishige. Jpn. J. Appl. Phys. 32 (1993): 2052.

[13] C. D. Lee, C. Park, H. J. Lee, K. S. Lee, S. J. Park, C. G. Park, S. K. Noh, and N. Koguchi. Jpn. J. Appl. Phys. 37 (1998): 7158.

[14] K. Watanabe, N. Koguchi, and Y. Gotoh. Jpn. J. Sppl. Phys. 39 (2000): L79.

[15] T. Chikyow, and N. Koguchi. Jpn. J. Appl. Phys. 29 (1990): L2093.

[16] N. Koguchi, K. Ishige, and S. Takahashi. J. Vac. Sci. & Technol. B11 (1993): 787.

[17] T. Chikyow, and N. Koguchi. Appl. Phys. Lett. 61 (1992): 2431.

[18] J. M. Lee, D. H. Kim, H. Hong, J. C. Woo, and S. J. Park. J. Cryst. Growth 212 (2000): 67.

[19] J. S. Kim, and N. Koguchi. Appl. Phys. Lett. 85 (2004): 5893.

[20] T. Mano, K. Watanabe, S. Tsukamoto, H. Fujioka, M. Oshima, and N. Koguchi. Jpn. J. Appl. Phys. 38 (1999): L1009 L 1011.

[21] Y. Horikoshi, M. Kawashima, and H. Yamaguchi. Jpn. J. Appl. Phys. 27 (1988): 169.

[22] Y. Horikoshi, M. Kawashima, and H. Yamaguchi. Jpn. J. Appl. Phys. 25 (1986): L868.

[23] P. Y. Yu, and M. Cardona. Fundamentals of semiconductors: physics and materials properties. 2 nd ed. Berlin: Springer-Verlag, 1999.

[24] C. Kittel. Introduction to solid state physics. 7 th ed. New York: Wiley, 1996.

[25] Pallab Bhattacharya. Semiconductor optoelectronic devices. New Jessy: Prentice-Hall. Inc, 1994.

[26] M.Sugawara. Theoretical Bases of the Optical Properties of Semiconductor Quantum Nano-Structures. In M. Sugawara (ed.). Semiconductors and semimetals vol.60: Self-Assembled InGaAs/GaAs Quantum Dots, pp.1-116. San Diego: Academic Press, 1999.

[27] D. Bimberg, M. Grundmann, and N. N. Ledentsov. Quantum dot heterostructures. Chichester: Wiley, 1999.

[28] G. Bastard, and J. A. Brum. Electronic states in semiconductor heterostructures. IEEE Journal of Quantum Electronics QE-22 (1986): 1625-1644.

[29] Y. Arakawa, and H.Sakaki. Multidimensional quantum well laser and temperature dependence of its threshold current. Appl. Phys. Lett. 40 (1982): 939.

[30] M. Asada, Y. Miyamoto, and Y. Suematsu. Gain and the threshold of three-dimensional quantum-box lasers. IEEE Journal of Quantum Electronics QE-22 (1986): 1915-1921

[31] Z. I. Alferov. the double heterostructure concept and its applications. Nobel Lecture. Reviews of Modern Physics 73 (2001): 767-782.

[32] A. E. Zhukov, et al. 3.5 W continuous wave operation from quantum dot laser. Materials Science and Engineering B 74 (2000): 70-74.

[33] M. bayer, M. Korkisinski, P. Hawrylak, T. Gutbrod, M. Michel, and A. Forchel. Phys. Rev Lett. 90 (2003): 186801.

[34] E. Ribeiro, A.O. Govorov, W. Carvalho Jr., and G. Medeiros-Ribeiro. Phys. Rev. Lett. 92 (2004): 126402.

[35] K. A. Cheng, and C. H. Yang. Nanometer-size InAs/AlSb quantum wires: Fabrication and characterization of Aharonov–Bohm quantum rings. J. Appl. Phys. Vol. 88 No.9 (2000): 5272-5276.

[36] M. Manninen, P. Koskinen, M. Koskinen, S. Viefers, and S.M. Reimann. Energy spectra and electron localization in quantum rings and dots.

[37] M. A. Herman, and H. Sitter. Molucular beam epitaxy fundamentals and current status. Berlin: Spinger-Verlag, 1989.

[38] W. Seifert, et al. In-situ growth of quantum dot structures by the Stranski-Krastanow growth mode. Crystal Growth and Characterization 33 (1996): 423-471.

[39] E. P. O'Reilly. Valence band engineering in strained-layer structures. Semiconductors Science and Technology 4 (1989): 121-137.

[40] T. Mano, and N. Koguchi. J. Crystal Growth 278 (2005): 108-112.

[41] T. Mano, K. Watanabe, S. Tsukamoto, H. Fujioka, M. Oshima, and N. Koguchi. J. Crystal Growth 209 (2000): 504.

List of Publications

1. InGaAs/GaAs ring-like nanostructures grown by droplet using molecular beam epitaxy, Naraporn Pankaow, Somsak Panyakeow and Somchai Ratanathummaphan, 19th International Conference on Indium Phosphide and Related Materials (IPRM'07), Kunibiki Messe, Matsue, Japan, 14-18 May, 2007.

2. Nanometer-scale $In_{0.5}Ga_{0.5}As$ ring-like structure grown by droplet epitaxy, Naraporn Pankaow, Somsak Panyakeow and Somchai Ratanathummaphan, 4th International Conference on Materials for Advanced Technologies (ICMAT 2007), Singapore International Convention & Exhibition Centre, Singapore, 1-6 July,2007.

VITAE

Naraporn Pankaow was born in Bangkok, Thailand on October 15th, 1983. She graduated from Chulalongkorn university demonstration in March 2001. In June 2001, she entered Chulalongkorn University and received the Bachelor of Engineering in field of Electrical Engineering with GPAX 3.35 in April 2005. She was further her study in October 2005, as a master student.